Special Feature: Materials Analysis

Review

A Powerful Tool to Characterize Lithium Insertion Materials for Advanced Lithium-ion Batteries: Macro- and Microscopic Magnetism Studied by Magnetic Susceptibility (χ) and Muon-spin Rotation/Relaxation (μSR) Measurements

Kazuhiko Mukai

Report received on Oct. 20, 2011

ABSTRACT The macroscopic magnetism of lithium insertion materials for lithium-ion batteries is investigated using magnetic susceptibility (χ) measurements to obtain an insight into the interrelationship between the electrochemical, structural, and magnetic properties. A new technique of muon-spin rotation/relaxation (μSR) measurements is also introduced to determine the microscopic magnetism of lithium insertion materials. Here we report results on two structural types; the layered structure of $LiCo_{1-x}Ni_xO_2$ and the spinel-framework structure of $Li[M_xMn_{2-x}]O_4$ with M = Li, Mg, and Ni.

KEYWORDS Lithium-ion Battery, Lithium Insertion Material, Electric Vehicle, Magnetic Susceptibility (χ), Muon-spin Rotation/Relaxation (μSR), Layered Structure, Spinel-framework Structure

1. Introduction

Over the past one hundred years, the internal-combustion engine system has been used as a power supply for vehicles. However, recent issues such as global warming, environmental pollution, and consumption of fossil fuel have prompted the production of more efficient and clean vehicles. One of the ultimate solutions is the electric vehicle (EV), which is powered by an electric motor with a rechargeable battery, because the EV needs no fuel, and exhausts no harmful gases such as nitrogen oxides (NO_x) and sulfur oxides (SO_x). Furthermore, battery charging during the night time enables load balancing of the electrical power supply. There is no doubt that the performance of the rechargeable batteries used determines the performance of EV. Compared with rechargeable batteries such as lead-acid and nickel-metal hydride (Ni-MH) batteries, lithium-ion batteries (LIB) have attracted significant interest from battery researchers and electrochemists due to their high-energy density and wide variety of positive/negative electrode materials.[1] **Figure 1** shows a schematic illustration of the operation principle of the LIB, which consists of two insertion electrode materials and a non-aqueous electrolyte. Lithium ions move back and forth between the positive and negative electrode materials during charge and discharge reactions. Electrons are simultaneously extracted from one electrode and injected into the other, storing and releasing electrical

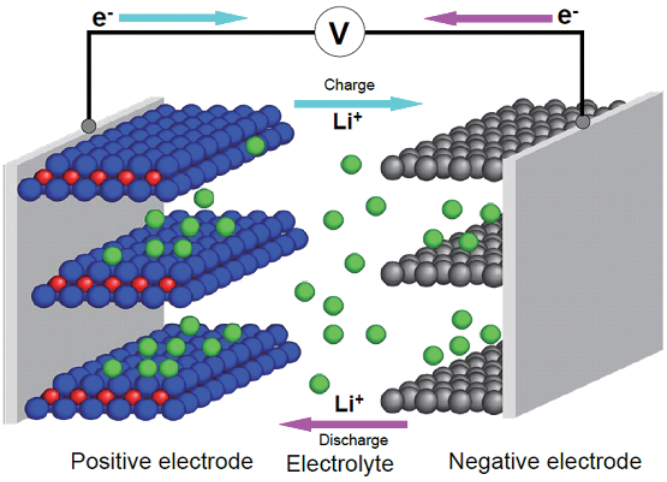

Fig. 1 Schematic illustration of the LIB operation principle. When the battery is charged, lithium ions in the positive electrode move to the negative electrode through the electrolyte. During discharge, lithium ions in the negative electrode return to the positive electrode, and discharge current flows. Thus, the LIB is charged and discharged only through the movement of lithium ions.

energy. Surprisingly, the framework structure of the lithium insertion material is maintained during the overall reaction. This reaction is referred to as *topotactic*, where *topo* and *tactic* mean 'place' and 'spatial arrangement', respectively, and this is a reason why LIBs can be used for more than one thousand cycles.

The commercial LIB is based on the report by Goodenough and co-workers; lithium cobalt oxide $LiCoO_2$, having a layered structure with a space group of $R\bar{3}m$ (see **Fig. 2**(a)), shows an operation voltage around 4 V vs. Li^+/Li.[2] In 1991, Sony Corporation released a 750 mAh class LIB by selecting $LiCoO_2$ and petroleum coke as battery materials.[3] The rechargeable capacity of $LiCoO_2$ is limited to ca. 140 $mAh \cdot g^{-1}$ due to its structural instability;[4,5] therefore, possible alternatives to $LiCoO_2$, such as $LiNiO_2$,[6-8] $LiCo_{1-x}Ni_xO_2$,[9,10] $Li[Li_xMn_{2-x}]O_4$,[11-13] $Li[Ni_{1/2}Mn_{3/2}]O_4$,[14-16] and $LiFePO_4$,[17,18] have been investigated over the past decades. However, the current LIB positive electrode materials consist mainly of the following 10 elements; Li, C, O, Al, P, Co, Mn, Fe, Co, and Ni, because of their high energy density, low toxicity, and inexpensive material cost. Thus, in order to find advanced lithium insertion materials by combination of these limited elements, we must understand the correlation between the fundamental physical (e.g. magnetic, electronic, and mechanical) properties and electrochemical properties of the materials currently used.

Among the many methods to characterize lithium insertion materials, magnetic susceptibility (χ) measurement is a powerful tool to investigate the local structural environment. χ measurements of $LiCo_{1-x}Ni_xO_2$ with $x \geq 0.85$ has revealed the presence of a small amount of Ni ions in the Li layer, although conventional X-ray diffraction (XRD) measurements fail to detect the Ni ions in the Li layers of these compounds.[8,19,20] In addition, the muon-spin rotation/relaxation (μSR) technique can be applied to research on lithium insertion materials, because an antiferromagnetic order is partially observed in stoichiometric $LiCoO_2$ below 30 K,[21] while $LiCoO_2$ was believed to be paramagnetic state down to 5 K according to χ[22] and ^{7}Li- nuclear magnetic resonance (NMR)[23] measurements due to non-magnetic Co^{3+} ions with $S = 0$ ($t_{2g}^6 e_g^0$). Here, μSR is very sensitive to local magnetic environments and is a powerful technique to detect both static and dynamic internal magnetic fields from 0.1 Oe to 100 kOe caused by nuclear- and electronic-magnetic moments.[24]

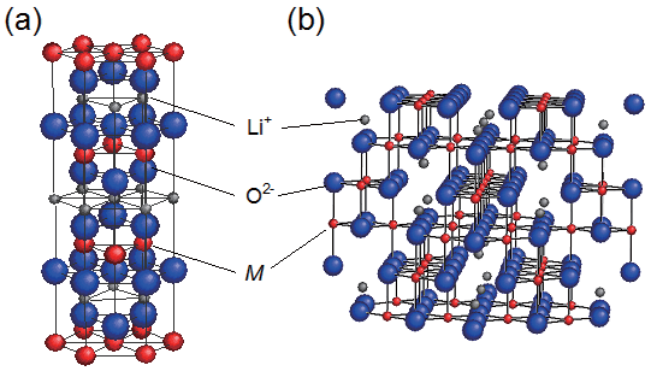

Fig. 2 Crystal structures of (a) $LiMO_2$ and (b) LiM_2O_4 lithium insertion materials, where M is a 3d transition metal such as Ni, Co, and Mn. $LiMO_2$ has a layered structure with a space group of $R\bar{3}m$, whereas LiM_2O_4 is a spinel-framework structure with a space group of $Fd\bar{3}m$.

Figure 2 shows that the crystal structure of lithium insertion materials can be mainly classified into two categories; one is $LiMO_2$ with a layered structure ($R\bar{3}m$) (Fig. 2(a)) and the other is LiM_2O_4 with a spinel-framework structure ($Fd\bar{3}m$) (Fig. 2(b)), where M is a 3d transition metal, such as Co, Ni, and Mn. In the $LiMO_2$ structure, to which $LiCoO_2$, $LiNiO_2$, and $LiCo_{1-x}Ni_xO_2$ ($0 < x < 1$) belong, Li^+ ions and M ions occupy the octahedral 3b and 3a sites, respectively, in a cubic closed-packed (*ccp*) oxygen array. In contrast, the LiM_2O_4 structure, which includes compositions such as $LiMn_2O_4$, $Li[Li_xMn_{2-x}]O_4$ ($0 \leq x \leq 1/3$), and $Li[Ni_{1/2}Mn_{3/2}]O_4$, the Li^+ ions and M ions are situated on the tetrahedral 8a and octahedral 16d sites, respectively, in the *ccp* oxygen array. In $LiMO_2$, Li^+ ions can move in the x and y directions, i.e., $LiMO_2$ has two-dimensional (2D) ion channels, while LiM_2O_4 has 3D channels. Furthermore, with respect to magnetism, $LiMO_2$ exhibits a 2D geometrical spin frustration, while LiM_2O_4 has a 3D geometrical spin frustration. In this paper, we report on results from systematic χ and μSR studies of these compounds to clarify the interrelationship between the electrochemical, structural, and magnetic properties of lithium insertion materials. In section 3.1, the electrochemical properties of the layered Li_xCoO_2 and Li_xNiO_2 compounds are correlated to a magnetic phase diagram combined with the change in crystal structure with x. In sections 3.2 and 3.3, respectively, the microscopic structural nature of the $Li[Li_xMn_{2-x}]O_4$ and $Li[Ni_{1/2}Mn_{3/2}]O_4$ spinels are described to provide an understanding of the homogeneity/inhomogeneity of the sample through its

microscopic magnetism. Finally, the difference between the layered Li_xNiO_2 and the $Li_xMn_2O_4$ spinel during the delithiation reaction is discussed in section 3.4.

2. Experimental

2. 1 Sample Preparation

Powder samples of $LiCo_{1-x}Ni_xO_2$ with $0 \le x \le 1$,[25-33] $Li[Li_xMn_{2-x}]O_4$ with $0 \le x \le 1/3$,[34,35] $Li[Mg_xMn_{2-x}]O_4$ with $0 \le x \le 1/2$,[36] and $Li[Ni_{1/2}Mn_{3/2}]O_4$[37,38] were prepared by solid-state reaction. For the $LiCo_{1-x}Ni_xO_2$ samples, a mixture of $LiNO_3$ (Li_2CO_3 for $x = 1$), $NiCO_3$, and $CoCO_3$ powders was well mixed and pressed into a pellet of 23 mm diameter and ca. 5 mm thickness. The pellet was then heated in the temperature (T) range between 750 and 900°C in an oxygen (in air for $x = 1$) flow for 12 h.[25-33] For the $Li[Li_xMn_{2-x}]O_4$, $Li[Mg_xMn_{2-x}]O_4$, and $Li[Ni_{1/2}Mn_{3/2}]O_4$ samples, a two-step solid-state reaction[15,39] was employed to obtain highly crystallized samples with an octahedral crystal habit. In the first step, the crystallization process is completed at high T around 1000°C, and then in the second step, the chemical composition is controlled precisely below 700°C. For the $Li[Li_xMn_{2-x}]O_4$ samples with $0 \le x \le 1/3$, a reaction mixture of $LiOH \cdot H_2O$ and MnOOH (manganite) was heated at 1000°C in air for 12 h, and then oxidized at 700°C for $x = 0$, 600°C for $x = 0.1$, 550°C for $x = 0.2$ in air for 12 h. Only for the $x = 1/3$ sample, the pellet was oxidized at 650, 600, 550, and 500°C in air for 24 h without cooling to room T.[35] For the $Li[Mg_xMn_{2-x}]O_4$ samples with $0 \le x \le 1/2$, a mixture of $LiOH \cdot H_2O$, $Mg(OH)_2$, and MnOOH was heated at 1000°C for 12 h, then oxidized at 700°C in an oxygen flow.[36] Two structural types of $Li[Ni_{1/2}Mn_{3/2}]O_4$ were prepared;[37,38] the "cation-disordered" $Li[Ni_{1/2}Mn_{3/2}]O_4$ was synthesized by heating a mixture of $LiOH \cdot H_2O$ and nickel manganese hydroxide at 1000°C for 12 h, and the "cation-ordered" $Li[Ni_{1/2}Mn_{3/2}]O_4$, i.e., $Li[Ni_{1/2}Mn_{3/2}]O_4$ ($P4_332$), was prepared by annealing the cation-disordered $Li[Ni_{1/2}Mn_{3/2}]O_4$ below 700°C. The obtained powders were characterized using powder XRD (RINT-2200, Rigaku Co. Ltd., Japan) and inductively coupled plasma-atomic emission spectroscopy (ICP-AES, CIROS 120, Rigaku Co. Ltd., Japan).

The electrochemical reactivity was examined in a non-aqueous lithium cell. For preparation of the electrode, poly-vinylidene fluoride (PVdF) dissolved in *N*-methyl-2-pyrrolidone (NMP) solution was used as a binder. The black viscous slurry, consisting of 88 wt% active material, 6 wt% acetylene black, and 6 wt% PVdF, was cast on an aluminum foil with a blade. NMP was evaporated at 120°C for 30 min, and the electrode (⌀15 mm) was then dried under vacuum at 150°C for 12 h. The counter electrode (⌀19 mm) was prepared by pressing lithium metal onto a stainless steel substrate. Two sheets of porous polypropylene membrane (Celgard 2500) were used as a separator. 1 M $LiPF_6$ dissolved in ethylene carbonate (EC)/dimethyl carbonate (DMC) (3:7 volume ratio) solution was used as the electrolyte. For the electrochemical tests, the current applied to the cell was 0.5 (or 0.3) mA, which corresponds to a current density of ca. 0.28 (or 0.17) $mA \cdot cm^{-2}$.

Delithiated samples for the χ and μSR measurements were prepared by two different methods; by electrochemical reaction in a non-aqueous lithium cell[26-29,32,33,37] and by chemical reaction.[40-42] For the electrochemical reaction, the pressed powder and a lithium metal sheet were used as working and counter electrodes, respectively. To avoid signals from the conducting additives and binder, the electrode was made entirely from the active material. For the chemical reaction, 2 g of $LiNiO_2$ (3.6 g of $LiMn_2O_4$) powder was immersed into 100 mL of HNO_3 solution and then stirred at room T for 24 h. After the acid treatment, the sample was filtered and dried at 40°C (60°C for $LiMn_2O_4$) in an air-oven.

2. 2 Magnetic Measurements

DC-magnetic measurements were carried out using a superconducting quantum interference device (SQUID) magnetometer (MPMS, Quantum Design) in the T range between 5 and 700 K under a magnetic field $H \le 55$ kOe. The magnetic measurements provide the equilibrium value of magnetization (M) in a sample.[43,44] The sample is magnetized under constant T and H, and T dependence of the magnetic susceptibility χ (= M/H) and a magnetization curve $M(H)$ are obtained. The sample was packed into two sheets of aluminum foil (20× 20 mm), attached to the SQUID sample rod with a copper wire, and then finally installed into the sample chamber. The sample was firstly cooled to 5 K and a magnetic field (H = 10 kOe) was applied using the "no overshoot" mode, in which the field oscillation is suppressed. After adjusting the sample position to the center of the SQUID coils,

measurements were performed with movement of the sample position. For the delithiated samples, the sample was removed from the lithium cell in an argon-filled glovebox just before χ measurements.

The μSR experiment was performed at TRIUMF in Canada, Paul Scherrer Institut (PSI) in Switzerland, and Rutherford Appleton Laboratory (RAL) in UK. A muon is an elementary particle with spin 1/2 and gyromagnetic ratio $\gamma_\mu/2\pi$ = 13.554 kHz/Oe. When ca. 100% polarized muons are implanted into a sample, the muon spin precesses by the local magnetic field of the sample. The unstable muons soon decay into positrons (the muon lifetime is 2.2 μs). The decay positron is then emitted preferentially along the muon spin direction. By collecting several million positrons as a function of the evolution time, the time (t) dependence of the muon-spin polarization ($A_0P(t)$) can be constructed, where A_0 is the initial asymmetry and $P(t)$ is the polarization function. Zero-field (ZF)-μSR is a very sensitive method used to detect weak internal magnetism that arises due to ordered magnetic moments or random fields that are static or fluctuating with time. Weak-transverse-field (wTF)-μSR, which involves the application of an external magnetic field perpendicular to the initial muon spin, is suitable for investigating the presence/absence of magnetic transition T, and the volume fraction of paramagnetic phases in the sample. More details regarding μSR technique are reported elsewhere.[24,45] Approximately one gram of sample was pressed into a pellet (⌀15 mm diameter, ca. 1 mm thick) and placed in the sample holder of a cryostat. The delithiated samples were removed from the lithium cell to a sealed sample cell in a He-filled glove-box, and then the sample cell was placed onto the sample holder of the cryostat. After the μSR measurements, the delithiated sample was returned to the lithium cell to evaluate the open circuit voltage (OCV) and confirm the stability of the sample during the μSR measurement.

3. Results and Discussion

3. 1 Magnetism of $LiCo_{1-x}Ni_xO_2$ with $0 \le x \le 1$[25-33]

Both $LiCoO_2$ and $LiNiO_2$ adopt a layered structure with $R\bar{3}m$ space group, so that $LiCo_{1-x}Ni_xO_2$ is a solid solution between $LiCoO_2$ and $LiNiO_2$ in the entire x range.[6-10] However, with respect to μSR, the magnetism of $LiCoO_2$ is very different from that of $LiNiO_2$, in that long-range antiferromagnetic (AF) ordering is observed below 30 K, probably due to a charge disproportionation reaction of the non-magnetic Co^{3+} ions ($2Co^{3+} \rightarrow Co^{2+} + Co^{4+}$).[21] In contrast, no long-range magnetic ordering is observed for $LiNiO_2$, but a fast spin-glass-like fluctuation in $Li_{0.98}Ni_{1.02}O_2$ is observed even at 2 K.[46] Considering the structural features of the $Co_{1-x}Ni_xO_2$ plane, cations are likely to become ordered, although it is not impossible, but very difficult, to detect the (short-range) ordering by XRD. Therefore, systematic μSR measurements of powder $LiCo_{1-x}Ni_xO_2$ samples were conducted to elucidate the microscopic magnetism.

Figure 3 shows ZF-μSR spectra for the $LiCo_{1-x}Ni_xO_2$ samples with x = 0, 0.25, 0.5, 0.75, and 1 at 1.8 K in the time domain below (a) 10 and (b) 1 μs. The ZF-μSR spectrum for $LiCoO_2$ (x = 0) shows mainly a slow relaxation with a broad minimum at ca. 4 μs, which is a typical Kubo-Toyabe[47] (KT) signal due to randomly oriented nuclear magnetic moments of ^{7}Li (4.24 μ_N) and ^{59}Co (5.25 μ_N). However, a fast relaxation signal appears in the early time domain below ca. 0.2 μs (see Fig. 3(b)), due to the formation of a static AF ordered phase below 30 K. On the other hand, the ZF-μSR spectra for samples with x = 0.25, 0.5, and 0.75 show a rapid relaxation without an oscillation in the time domain below ca. 0.3 μs, which suggests that the muon spins are depolarized by disordered magnetic moments of Ni^{3+} ions with S = 1/2 ($t_{2g}^6 e_g^1$). The ZF-μSR spectrum for the x = 1 sample is so strongly damped, which

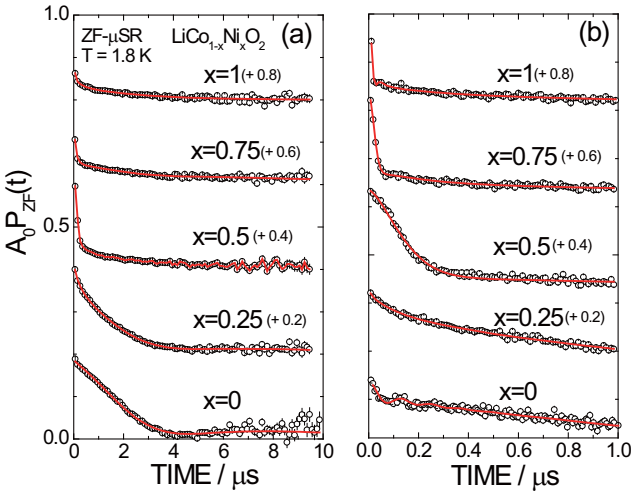

Fig. 3 ZF-μSR spectra for $LiCo_{1-x}Ni_xO_2$ samples with x = 0, 0.25, 0.5, 0.75, and 1 in the time domain below (a) 10 and (b) 1 μs. The solid lines indicate the fitting results using Eq. (1). The top four ZF-μSR spectra are shifted upwards by + 0.2 for clarity.

indicates that the Ni moments freeze in a highly disordered fashion, as in the case for $Li_{0.98}Ni_{1.02}O_2$.[46] As a result, the ZF-μSR spectra for $LiCo_{1-x}Ni_xO_2$ are well fitted by a combination of four signals; an exponentially relaxing cosine oscillation signal due to AF ordering for $LiCoO_2$, a KT signal due to randomly oriented nuclear moments, an exponentially relaxing non-oscillatory signal due to localized disordered moments, and a zeroth-order Bessel function of the first kind $J_0(\omega_\mu t)$, which describes the fast relaxation behavior for $LiNiO_2$:[25-28,30,32,33]

$$A_0P_{ZF}(t) = A_{AF}\cos(\omega_{AF}t+\varphi)\exp(-\lambda_{AF}t) + A_{KT}G^{DGKT}(\Delta,\nu,t) + A_{fast}\exp(-\lambda_{fast}t) + A_{IC}\exp(-\lambda_{IC}t)J_0(\omega_{IC}t), \quad \cdots\cdots\cdots\cdots\cdots (1)$$

where A_{AF}, A_{KT}, A_{fast}, and A_{IC} are the asymmetries of the four signals, λ_{AF}, λ_{fast}, and λ_{IC} are their relaxation rates, ω_{AF} is the muon Larmor frequency, ϕ is the initial phase of the precession, Δ is the field distribution width of the local fields at the disordered sites, and ν is the field fluctuation rate. When $\nu = 0$, a dynamic KT function, $G^{DGKT}(t, \Delta, \nu)$, is the static Gaussian KT function $G_{zz}^{KT}(\Delta, t)$ given by[47]

$$G_{zz}^{KT} = 1/3 + 2/3(1-\Delta^2t^2)\exp(-\Delta^2t^2/2) \quad \cdots\cdots (2)$$

A linear relation is obtained in the $\log(\lambda_{fast})$ versus x curve, where λ_{fast} increases exponentially with increasing x, which suggests a significant role of Ni^{3+} moments on λ_{fast}.[30] In addition, the magnitudes of the spin-glass-like transition temperature T_f, effective magnetic moment μ_{eff}, and Curie-Weiss temperature Θ_p, vary almost linearly with x,[31] which suggests that the change of magnetic properties with x in $LiCo_{1-x}Ni_xO_2$ is explained by an increase in the quantity of Ni^{3+} ions with $S = 1/2$ ($t_{2g}^6e_g^1$). Thus, the Co^{3+} and Ni^{3+} ions are homogeneously distributed in the $LiCo_{1-x}Ni_xO_2$ lattice even in a few angstrom.[30]

Li_xCoO_2 exhibits structural variation with x at ambient T (shown in later in Fig. 5(a)); as x decreases from 1, Li_xCoO_2 consists of a mixture of two rhombohedral ($R\bar{3}m$) phases for $0.95 > x \geq 0.75$, a rhombohedral phase for $0.75 > x \geq 0.56$ ($R\bar{3}m$), a monoclinic phase ($C2/m$) for $0.56 > x \geq 0.51$, and finally a rhombohedral phase at $x < 0.51$ ($R\bar{3}m$).[4,5] Moreover, the crystal structure of Li_xNiO_2 is dependent on x at ambient T. As x decreases from 1, the rhombohedral ($R\bar{3}m$) phase is stable down to $x = 0.75$, whereas the monoclinic phase ($C2/m$) is stable in the x range between 0.75 and ca. 0.45. As x is decreased further, the rhombohedral ($R\bar{3}m$) phase appears again for $0.45 > x \geq 0.25$, and finally two rhombohedral ($R\bar{3}m$) phases coexist at $x < 0.25$.[7,48,49] In order to clarify the correlation between the structural and magnetic properties of Li_xCoO_2 and Li_xNiO_2, the macro- and microscopic magnetism for the electrochemically delithiated Li_xCoO_2 and Li_xNiO_2, samples were investigated using χ and μSR measurements.

Figure 4(a) shows the T dependence of χ for the Li_xCoO_2 samples with $1 \geq x \geq 0.1$. The $\chi(T)$ curves for the samples with $x = 0.1$ and 0.44 are almost T-independent down to ca. 50 K, which suggests that the samples are Pauli-paramagnetic. The $\chi(T)$ curves for the samples with $0.75 \geq x \geq 0.49$ also exhibit Pauli-paramagnetic behavior down to ca. 170 K, and then χ suddenly decreases and reaches a broad minimum at ca. 100 K with further decrease in T. The cusp around 170 K was also reported for $x = 0.7$ and 0.95;[21] the cusp appears in a wide range of x between 0.95 and 0.5.[26,27] According to χ measurements in both zero-field-cooling (ZFC) and field-cooling (FC) modes with $H = 100$ Oe and 10 kOe, the cusp around 170 K is not

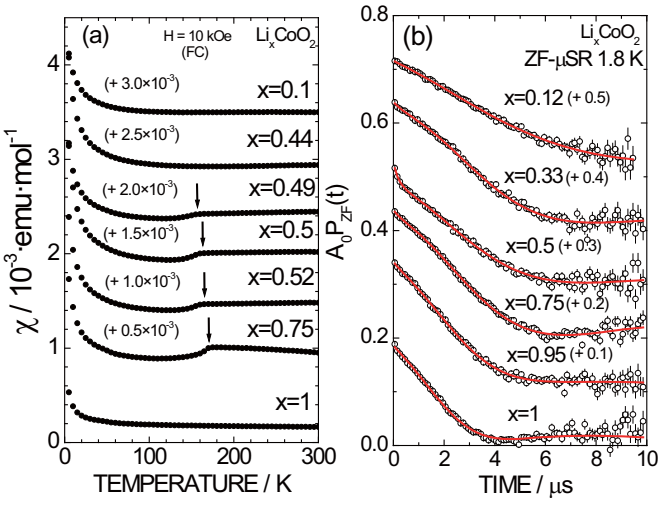

Fig. 4 (a) Temperature dependence of χ and (b) ZF-μSR spectra at 1.8 K for Li_xCoO_2 samples with $1 \geq x \geq 0.1$. χ was measured in FC mode with $H = 10$ kOe. The solid lines in (b) represent the fitting results from Eq. (3). The top six $\chi(T)$ curves and five ZF-μSR spectra are shifted upwards by $+ 0.5 \times 10^{-3}$ and + 0.1, respectively, for clarity.

thought to be a typical ferromagnetic (FM), ferrimagnetic, and/or spin-glass-like transition.[27] In addition, wTF-μSR measurements indicate that the x = 0.5 sample is in a PM state down to ca. 20 K.[27] Therefore, the cusp is thought to be a structural phase transition, a spin-state transition, and/or charge-ordering. Recent low-T XRD measurements revealed a structural phase transition around 170 K.[29] Figure 4(b) shows the ZF-μSR spectra for the Li_xCoO_2 samples with $1 \geq x \geq 0.12$ measured at 1.8 K. An oscillatory signal due to the formation of AF ordering disappears even for the x = 0.95 sample, and in turn, a slow relaxation signal due to the randomly oriented nuclear magnetism is observed for the $x < 1$ samples. The ZF-μSR spectra for $x < 1$ is well fitted by a combination of a dynamic KT[47] function $G^{DGKT}(t, \Delta, \nu)$ and an offset signal due to the Ag sample cell.

$$A_0 P_{ZF}(t) = A_{KT} G^{DGKT}(\Delta, \nu, t) + A_{BG} \exp(-\lambda_{BG} t) \quad \cdots\cdots\cdots\cdots\cdots (3)$$

where A_{BG} is the asymmetry of the background signal and λ_{BG} is its relaxation rate. Note that a fast relaxation signal is observed only for the x = 0.5 sample in the time domain below 1 μs. However, the volume fraction of the fast relaxation signal is ca. 25%, even at 1.8 K, which indicates that most of the sample is in the PM state down to 1.8 K.

Figure 5 shows a schematic illustration of the (a) electrochemical reaction scheme and (b) magnetic phase diagram determined from χ and μSR measurements for Li_xCoO_2. Static AF ordering is observed only for the x = 1 sample below 30 K, but the volume fraction is ca. 10%. All the Li_xCoO_2 samples with $x < 1$ exhibit Pauli PM behavior even at 1.8 K. Thus, even if the average valence of Co ions and the crystal structure of Li_xCoO_2 change with decreasing x, the magnetism of Li_xCoO_2 does not vary dramatically. Note that the magnetism of Li_xCoO_2 is quite different from those of A_xCoO_2 (A = Na and K), although Na_xCoO_2[50,51] and K_xCoO_2[52,53] exhibit static AF ordering accompanied with structural phase transitions. The crystal structure of Li_xCoO_2 with $x < 0.25$ belongs to a rhombohedral or monoclinic phase with the *ccp* structure, while those of Na_xCoO_2 and K_xCoO_2 are hexagonal close-packed (*hcp*) structures. This indicates that the arrangement of Co ions along the c-axis in Li_xCoO_2 is different from those in Na_xCoO_2 and K_xCoO_2; in the former, Co ions locate at the center of the Co triangular lattice, but in the latter two, the Co ions locate at the same (x, y) position to those in the neighboring CoO_2 plane. Therefore, the stacking sequence along the c-axis is thought to be crucial to determine the formation of AF ordering in A_xCoO_2.[25-27]

Figure 6 shows the ZF-μSR spectrum for the Li_xNiO_2 sample with x = 0.75 at 1.8 K. The ZF-μSR spectrum at 45 K exhibits KT behavior, which indicates that the sample is in a PM state (not shown). However, the ZF-μSR spectrum at 1.8 K has a damped oscillation, which indicates the formation of static AF ordering. The fit using a cosine oscillation ($\exp(-\lambda t)\cos(\omega_\mu + \phi)$) yields a delay of the initial phase (ϕ) by ca. –40°, which is physically meaningless. Thus, the ZF-μSR spectrum is fitted by a zeroth-order Bessel function $J_0(\omega_\mu t)$, as in the case for $LiNiO_2$, which describes the muon polarization evolution in an incommensurate (IC-) field distribution.

$$A_0 P_{ZF}(t) = A_{IC} \exp(-\lambda_{IC} t) J_0(\omega_{IC} t) + A_{fast} \exp(-\lambda_{fast} t) + A_{slow} \exp(-\lambda_{slow} t), \quad \cdots\cdots\cdots\cdots\cdots (4)$$

where A_{IC}, A_{fast}, and A_{slow} are the asymmetries of the three signals and λ_{IC}, λ_{fast}, and λ_{slow} are their relaxation rates. As T decreases from 35 K, f_{IC}(= $\omega_{IC}/2\pi$) increases

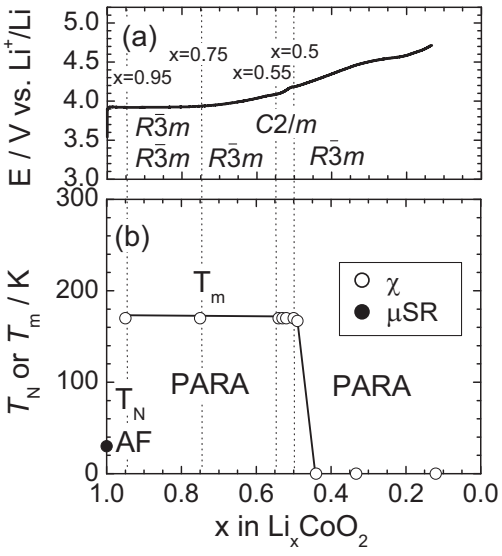

Fig. 5 Schematic illustration of (a) electrochemical reaction scheme and (b) magnetic phase diagram for Li_xCoO_2. T_m and T_N are magnetic transition temperatures determined from χ and μSR measurements, respectively. AF and PARA denote antiferromagnetism and paramagnetism, respectively.

rapidly with decrease in the df_{IC}/dT slope, and finally reaches ca. 30 MHz at 1.8 K, as expected for the ordering parameter of the AF transition. Considering the "1/3" tail component due to a polycrystalline sample ($A_{fast} + A_{slow}$), the normalized A_{IC} suggests that almost all the sample enters the AF phase below 35 K. Note that the ZF-μSR spectrum for $LiCo_{0.25}Ni_{0.75}O_2$ exhibits a spin-glass-like disordered magnetism (see Fig. 3), although the spin concentration on the two-dimensionally triangular lattice in $Li_{0.75}NiO_2$ is the same as that in $LiCo_{0.25}Ni_{0.75}O_2$; Ni^{3+} ions are magnetic with $S = 1/2$ ($t_{2g}^6 e_g^1$), while Ni^{4+} and Co^{3+} ions are non-magnetic with $S = 0$ ($t_{2g}^6 e_g^0$).[30]

The oscillatory signal is also observed for the Li_xNiO_2 samples with $x \geq 0.6$, which suggests the formation of static AF ordering. Although the AF structure is not fully understood at present, A-type AF ordering, i.e., FM in the plane, but AF between the plane, is most reasonable, as in the case for $NaNiO_2$.[54] This is because the Curie-Weiss temperature Θ_p, estimated from the $\chi(T)$ curves ranges between + 25 and + 60 K for the $x \geq 0.6$ samples, which suggests that the predominant interaction between Ni moments is FM.

The schematic magnetic phase diagram for Li_xNiO_2 is finally established from the χ and μSR measurements (see **Fig. 7**).[32,33] A dome-shaped AF phase region exists in the range of x between 1 and ca. 0.55, whereas the spin-glass-like phase appears at $0.55 \geq x \geq 0.1$. Note that χ measurements provide no information on the change in magnetic nature of Li_xNiO_2 with x; the magnitude of the spin-glass-like temperature T_f decreases almost linearly with decreasing x. Such a discrepancy between χ and μSR measurements is also observed for stoichiometric $LiCoO_2$[21,25-27] and low-dimensional systems such as $Ca_3Co_2O_5$.[55] This is because muons are influenced by the magnetic fields from nearest neighbors and are especially sensitive to short-range magnetic ordering that often appears in low-dimensional systems, whereas χ measurements mainly detect long range magnetic ordering. Furthermore, μSR measures fluctuating magnetic order/disorder on a muon time-scale (10^4-10^{12} s^{-1}), while (dc)-χ provides static information. Although the correlation between the solid-state electrochemistry and magnetism of Li_xNiO_2 is currently unclear, the present results demonstrate that μSR measurements are suitable to study the change in the physical/structural properties of Li_xNiO_2 during the charge/discharge reaction.

3. 2 Magnetism of $Li[Li_xMn_{2-x}]O_4$ with $0 \leq x \leq 1/3$[34,35]

In the crystal lattice of the $Li[Li_xMn_{2-x}]O_4$ (LMO)

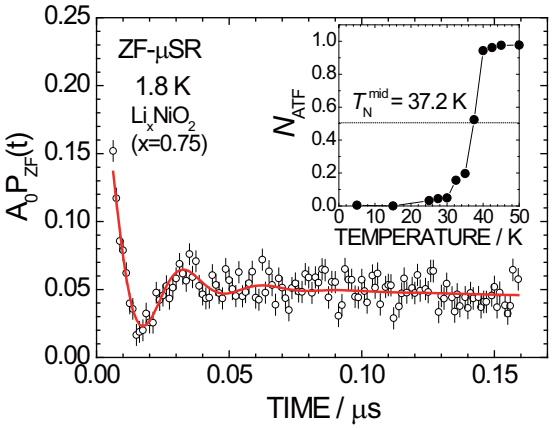

Fig. 6 ZF-μSR spectrum for the Li_xNiO_2 sample with x = 0.75 at 1.8 K. The solid line indicates the fitting result from Eq. (4). An oscillatory signal suggests the formation of static AF ordering in the sample. The temperature dependence of normalized weak-transverse-field asymmetry (N_{ATF}) is also shown in the inset. T_N^{mid} is the temperature at which $N_{ATF} = 0.5$.

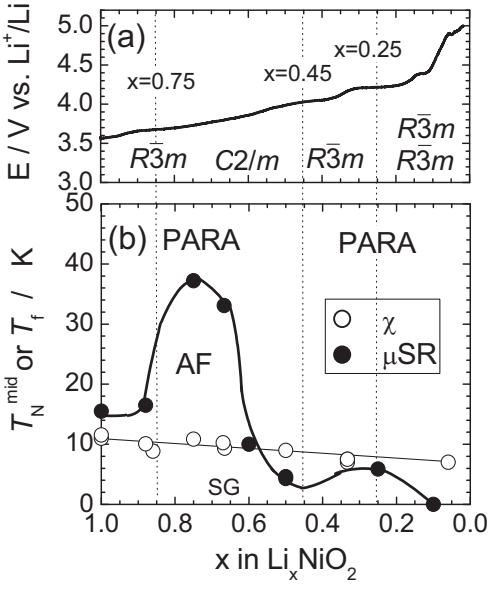

Fig. 7 Schematic illustrations of (a) the electrochemical reaction scheme and (b) magnetic phase diagram for Li_xNiO_2. T_f and T_N^{mid} are magnetic transition temperatures determined from χ and μSR measurements, respectively. PARA, AF, and SG denote paramagnetic, antiferromagnetic, and spin-glass-like phases, respectively.

spinel with space group $Fd\bar{3}m$, non-magnetic Li^+ ions locate at both tetrahedral 8*a* and 16*d* sites, while magnetic Mn^{3+} ions with $S = 2$ ($t_{2g}^3 e_g^1$) and Mn^{4+} ions with $S = 3/2$ ($t_{2g}^3 e_g^0$) occupy the octahedral 16*d* sites. The excess Li^+ ions at the 16*d* sites (x) not only dilute the magnetic interaction between Mn ions, but also increase the average valence of Mn ions (V_{Mn}^{ave}); $V_{Mn}^{ave} = 3.5$ for $LiMn_2O_4$, and as x increases from 0, V_{Mn}^{ave} increases in proportion to x, and reaches 4 for $Li[Li_{1/3}Mn_{5/3}]O_4$. We have performed χ and ZF-μSR measurements for samples with $0 \le x \le 1/3$ to elucidate the structural and physical properties of LMO. **Figures 8**(a) and (b) show the T dependence of the field distribution width Δ, and the muon fluctuation rate ν, for LMO samples with $x = 0$, 0.05, 0.1, and 0.15. Here, the values of Δ and ν are obtained by fitting the ZF-μSR spectra with a dynamic KT[47] function $G^{DGKT}(t, \Delta, \nu)$. For the $x = 0$ sample, as T increases from 100 K, Δ remains almost constant (ca. 0.17 μs^{-1}) up to ca. 280 K, then suddenly drops to ca. 0.1 μs^{-1} with further increase in T. On the other hand, ν for the $x = 0$ sample reaches a maximum around 280 K, and then increases with further increase in T. Stoichiometric $LiMn_2O_4$ is known to exhibit a structural phase transition from a high-T cubic phase ($Fd\bar{3}m$) to a low-T orthorhombic ($Fddd$) phase at T_{JT} ~ 280 K, induced by a cooperative Jahn-Teller (JT) distortion of Mn^{3+} ions.[56-58] Furthermore, the $\chi^{-1}(T)$ curve for the $x = 0$ sample exhibits a small cusp at ca. 280 K, as shown in Fig. 8(c), due to orbital ordering of Mn^{3+} ions at T_{JT}. Thus, the sudden decrease in Δ and the peak of the $\nu(T)$ curve around 280 K are naturally assigned as to the JT transition. This can be explained as the consequence of a critical slowing down toward T_{JT} due to spin-phonon interaction.[59] It should be noted that the sudden decrease in Δ and the peak of the $\nu(T)$ curve are still observed even for the $x = 0.15$ sample, although there are no anomalies in the $\chi^{-1}(T)$ curve. Therefore, μSR detects the appearance of a short-range cooperative JT distortion even in the sample with $x = 0.15$,[34] while macroscopic analyses such as XRD and differential scanning calorimetry (DSC) show that T_{JT} disappears at around $x = 0.035$.[56]

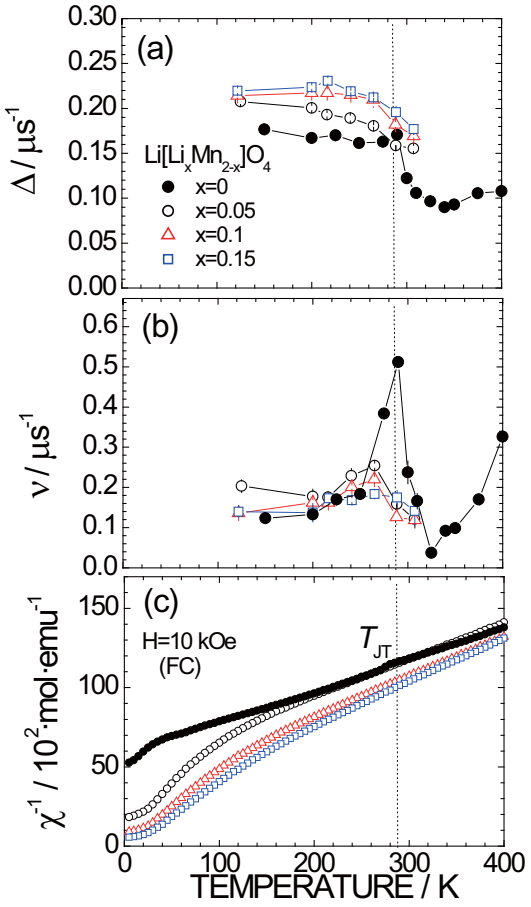

Fig. 8 Temperature dependence of (a) field distribution width (Δ), (b) field fluctuation rate (ν), and (c) inverse magnetic susceptibility (χ^{-1}) for $Li[Li_xMn_{2-x}]O_4$ samples with $x = 0$, 0.05, 0.1, and 0.15. The data was obtained by fitting the ZF-μSR spectra using a dynamic KT function. χ was measured in FC mode with $H = 10$ kOe. T_{JT} represents the transition temperature due to the cooperative Jahn-Teller (JT) distortion of Mn^{3+} ions with $S = 2$ ($t_{2g}^3 e_g^1$).

Figure 9 shows the charge and discharge curves of a lithium cell with the $x = 1/3$ sample. We assume that the theoretical charge/discharge capacity ($Q_{theo}(x)$) for LMO with $x > 0$ is determined by the following reaction:

$$Li[Li_xMn^{3+}_{1-3x}Mn^{4+}_{1+2x}]O_4 \rightarrow yLi^+ + ye^- + Li_{1-y}[Li_xMn^{3+}_{1-3x-y}Mn^{4+}_{1+2x+y}]O_4 \quad \cdots\cdots\cdots\cdots\cdots (5)$$

where $Q_{theo}(x)$ in mAh·g^{-1} is given by

$$Q_{theo}(x) = Q_{theo}(LiMn_2O_4) \times (1-3x) \times \frac{M(LiMn_2O_4)}{M(x)}, \quad \cdots\cdots\cdots\cdots\cdots (6)$$

where $Q_{theo}(LiMn_2O_4)$ is the theoretical charge/discharge capacity of $LiMn_2O_4$ (= 148 mAh·g^{-1}), and $M(LiMn_2O_4)$ and $M(x)$ are the molecular weights of $LiMn_2O_4$ and LMO with $x > 0$, respectively. This

means that $Q_{theo}(x)$ decreases linearly with increasing x, and finally reaches 0 mAh·g^{-1} at $x = 1/3$ (see Fig. 9(b)). However, as shown in Fig. 9(a), approximately 46 mAh·g^{-1} of rechargeable capacity is obtained for the $x = 1/3$ sample. Moreover, a difference between $Q_{theo}(x)$ and the charge capacity at the fist cycle (Q_{cha}) is evident at $x > 0.2$ (see Fig. 9(b)). The μSR signal roughly corresponds to the volume fraction of the magnetic phases in the sample; therefore, μSR measurements were conducted for the $x = 1/3$ and Li_2MnO_3 samples to clarify the homogeneity/inhomogeneity of the $x = 1/3$ sample through its microscopic magnetism.

Figure 10 shows ZF-μSR spectra measured at 1.8 K for the LMO samples with $x = 0$, 0.1, 0.2, and 1/3. The ZF-μSR spectra for the samples with $x \geq 0.2$ lack an oscillatory signal, but pose a first minimum at around $t = 0.015$ μs, which indicates a spin-glass-like freezing of the Mn moments at low T. On the other hand, a clear oscillation with an oscillation frequency $f = 42.3(3)$ MHz is observed for the $x = 1/3$ sample. XRD measurements indicate that the Li_2MnO_3 phase coexists in the $x = 1/3$ sample and that the weight fraction of the Li_2MnO_3 phase ($W_p(Li_2MnO_3)$) in the $x = 1/3$ sample is 11.0%. Furthermore, as shown in Fig. 10(e), the ZF-μSR spectrum for the Li_2MnO_3 sample has an oscillation signal with an oscillation frequency $f = 42.2(1)$ MHz. The oscillation is, thus, caused by the Li_2MnO_3 phase in the $x = 1/3$ sample. **Figure 11** shows the T dependence of normalized wTF asymmetries (N_{ATF}) for the LMO samples with $x = 0$, 0.1, 0.2, and 1/3 together with the result for Li_2MnO_3. Here, N_{ATF} corresponds to the volume fraction of PM phases in the sample; when $N_{ATF} = 1$, the entire sample is in a PM state, whereas when $N_{ATF} = 0$, the sample is in a magnetic phase such as FM, AF, or ferrimagnetic, spin-glass-like phases. A step-like decrease in N_{ATF} from 1 to 0 for the samples with $x \leq 0.2$ indicates the existence of a sharp magnetic transition for these samples. On the contrary, as T decreases from 50 K,

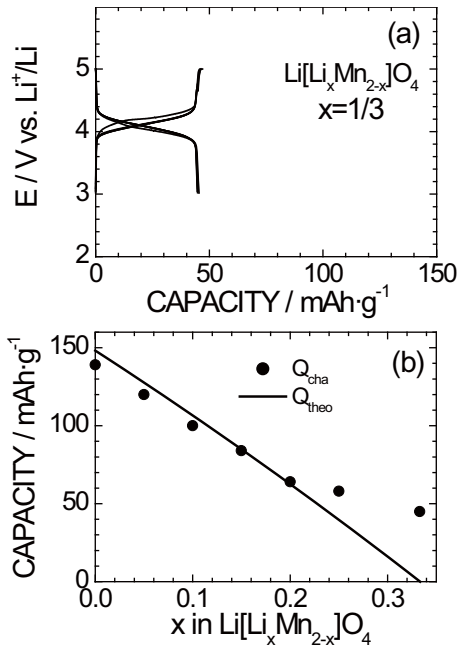

Fig. 9 (a) Charge and discharge curves of a lithium cell with $Li[Li_xMn_{2-x}]O_4$ (LMO) at $x = 1/3$. The cell was operated in the voltage range between 3 and 5 V at a current density of 0.17 mA·cm^{-2} at 25°C. A comparison of the theoretical charge/discharge capacity (Q_{theo}) and the experimental charge capacity at the first cycle (Q_{cha}) is shown in (b). Note that Q_{theo} should be 0 mAh·g^{-1} at $x = 1/3$ if it is assumed that the electrochemical reaction proceeds according to Eq. (5).

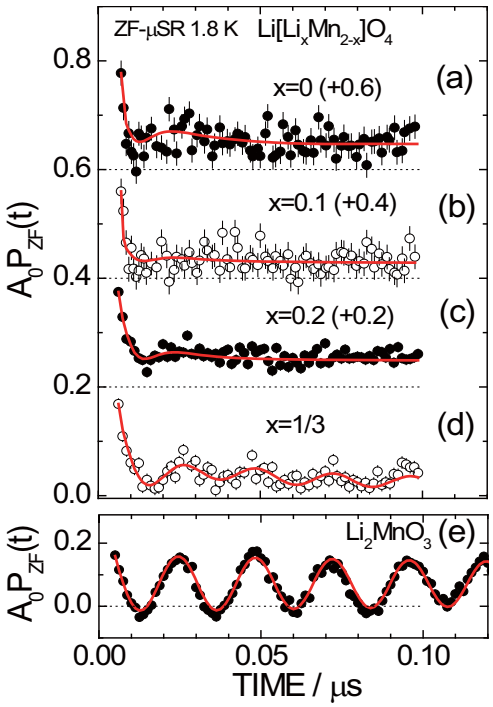

Fig. 10 ZF-μSR spectra at 1.8 K for $Li[Li_xMn_{2-x}]O_4$ with x = (a) 0, (b) 0.1, (c) 0.2, and (d) 1/3. The ZF-μSR spectrum for the Li_2MnO_3 sample is also shown in (e) for comparison. The top three ZF-μSR spectra are shifted upwards by + 0.2 for clarity. The powder sample of Li_2MnO_3 was prepared by heating a reaction mixture of $LiOH·H_2O$ and MnOOH at 900°C for 12 h.

N_{ATF} for the x = 1/3 sample decreases slightly around 36 K, then gradually decreases with further lowering of T. N_{ATF} for the Li_2MnO_3 sample exhibits a step-like decrease at 36 K due to the formation of AF ordering;[60] therefore, the small decrease at 36 K in the x = 1/3 sample is caused by the magnetic transition of Li_2MnO_3.

The x = 1/3 compound has been assigned as a mixture of a $Li[Li_xMn_{2-x}]O_4$ phase and a Li_2MnO_3 phase;[61-63] the actual chemical formula, especially at $x > 0.2$, is represented by

$$Li[Li_xMn_{2-x}]O_4 \leftrightarrow (1-z)Li[Li_{x-\omega}Mn_{1-2x+\omega}]O_4 + zLi_2MnO_3 + z/2O_2\uparrow \quad \cdots\cdots\cdots\cdots\cdots (7)$$

where

$$\omega = (x-z)/(1-z) \quad \cdots\cdots\cdots\cdots\cdots\cdots\cdots (8)$$

The chemical formula for the remaining spinel phase of the x = 1/3 sample is calculated to be $Li[Li_{0.21}Mn_{1.79}]O_4$ (ω = 0.124) using Eqs. (7) and (8) and $W_p(Li_2MnO_3)$ = 11.0%. Figure 11 shows that the x = 1/3 sample has a large magnetic transition width (ΔT_m ~ 28 K) compared to those for the x = 0.2 (ΔT_m ~ 5 K) and Li_2MnO_3 (ΔT_m ~ 2 K) samples. This indicates that the value of ω in the $Li[Li_xMn_{2-x}]O_4$ lattice is microscopically different, although XRD and neutron diffraction measurements have indicated that $Li[Li_{x-\omega}Mn_{2-x+\omega}]O_4$ is single-phase.[61-63] In other words, it is most likely that the inhomogeneous distribution of Li ions at the 16*d* sites correlates to the abnormal charge/discharge capacity for the x = 1/3 sample.[35] As pointed out by Paulsen and Dahn, the number of phases that can co-exist in the Li-Mn-O compound is estimated to be two, if the Gibbs phase rule is applied.[64] However, such multiple phases in the x = 1/3 sample suggest that rate of Eq. (7) is too slow to reach the thermodynamic equilibrium state. The inconsistency with the Gibbs phase rule prediction is also observed for fully delithiated Li_xNiO_2 with $x \leq$ 0.1; at least four different phases are present in the sample.[41,65,66] The composite compounds of $xLi_2MnO_3\cdot(1-x)LiMn_2O_4$[67] and/or $xLi_2MnO_3\cdot(1-x)LiMO_2$ with M = Co, Ni, and Mn[68,69] have recently been promising as positive electrode materials for high-energy density LIBs. Cation-ordering between Li and Mn ions, such as in the Li_2MnO_3 ($Li[Li_{1/3}Mn_{3/2}]O_2$) phase, is present in these compounds; therefore, μSR measurements would be useful to investigate the local structural environment in these compounds.

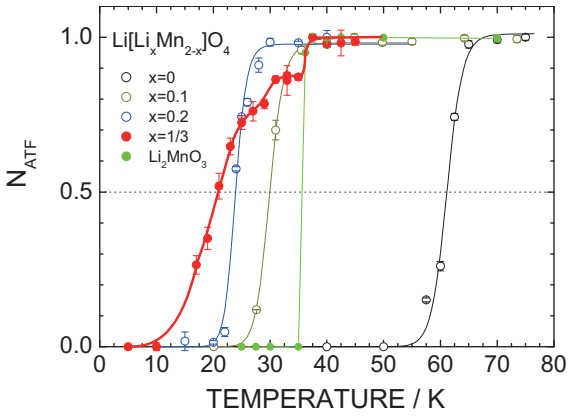

Fig. 11 Temperature dependence of the normalized wTF-asymmetries (N_{ATF}) for $Li[Li_xMn_{2-x}]O_4$ with x = 0, 0.1, 0.2, and 1/3, together with that for Li_2MnO_3.

3. 3 Magnetism of $Li[Ni_{1/2}Mn_{3/2}]O_4$[36-38]

Among the lithium manganese oxide spinels, $Li[Ni_{1/2}Mn_{3/2}]O_4$ is promising as a future positive electrode material, due to its high operating voltages around 4.7 V vs. Li^+/Li.[14-16] Stoichiometric $Li[Ni_{1/2}Mn_{3/2}]O_4$ (CO-LNMO) exhibits a 1:3 cation-ordering (CO) between Ni^{2+} and Mn^{4+} ions, which results in a superlattice structure that belongs to the $P4_332$ space group. However, cation-disordering (CDO) $Li[Ni_{1/2}Mn_{3/2}]O_4$ (CDO-LNMO) is easily formed depending on the reaction conditions.[14-16,39] The electrochemical properties of CDO-LNMO are different from those of CO-LNMO,[14-16,39] so that a quantitative indicator to identify the $Li[Ni_{1/2}Mn_{3/2}]O_4$ ($P4_332$) phase would be useful for optimization of the synthesis conditions. Therefore, χ measurements were conducted for both CO-LNMO and CDO-LNMO samples to clarify the inter-relationship between the magnetic and electrochemical properties of $Li[Ni_{1/2}Mn_{3/2}]O_4$.

Figure 12(a) shows charge/discharge curves of lithium cells with both CO-LNMO and CDO-LNMO samples. The charge/discharge curves for the CO-LNMO sample have a very flat operating voltage around 4.7 V. The rechargeable capacity in the voltage range between 3 and 5 V is 134 $mAh\cdot g^{-1}$, which corresponds to ca. 92% of the theoretical capacity calculated from the formula weight of $Li[Ni_{1/2}Mn_{3/2}]O_4$. In contrast, the charge/discharge curves for the CDO-LNMO sample are divided into

three distinct regions; a continuous change in voltage below ca. 4.6 V and two plateaus at around 4.6 and 4.7 V. The Fourier transform infrared (FTIR) spectrum for CO-LNMO indicates the existence of cation-ordering in the sample (see Fig. 12(b)). On the basis of factor group analysis,[70] IR active vibration modes for the $Fd\bar{3}m$ space group are predicted to be 4 ($4F_{1u}$), while those for the $P4_332$ group are expected to be 21 ($21F_1$). At least eight or more absorption bands appear only for the CO-LNMO sample, which indicates that its space group symmetry is lower than $Fd\bar{3}m$. Comparing the results reported previously for $Li[Ni_{1/2}Mn_{3/2}]O_4$,[14-16,39] CO-LNMO and CDO-LNMO samples are assigned as $Li[Ni_{1/2}Mn_{3/2}]O_4$ ($P4_332$) and cation-disordering $Li[Ni_{1/2}Mn_{3/2}]O_4$, respectively.

Figure 13 shows the T dependence of (a) χ, (b) χ^{-1}, and (c) $d\chi^{-1}/dT$ for the CO-LNMO and CDO-LNMO samples measured in FC mode with $H = 10$ kOe. χ for both samples rapidly increase below ca. 130 K with decreasing T, which suggests the appearance of spontaneous magnetization. Above 200 K, χ^{-1} increase with increasing T with a change in the $d\chi^{-1}/dT$ slope. For a PM state, the Curie-Weiss law in the general form is written as

$$\chi = \frac{N\mu_{\mathrm{eff}}^2}{3k_{\mathrm{B}}(T-\Theta_{\mathrm{p}})} + \chi_0, \quad \cdots\cdots\cdots\cdots\cdots (9)$$

where N is the number density of Ni and Mn ions, μ_{eff} is the effective magnetic moment of Ni and Mn ions, k_{B} is Boltzmann's constant, T is the absolute temperature, Θ_{p} is the Curie-Weiss temperature, and χ_0 is the temperature-independent susceptibility. Figure 13(c) shows that $d\chi^{-1}/dT$ is almost T-independent for both samples. The values of μ_{eff} and Θ_{p} are therefore calculated by fitting the $\chi(T)$ curves in the T range between 500 and 700 K, which gives $\mu_{\mathrm{eff}} = 3.78(1)\ \mu_{\mathrm{B}}$ and $\Theta_{\mathrm{p}} = -67(3)$ K for the CDO-LNMO sample, and $\mu_{\mathrm{eff}} = 3.50(1)\ \mu_{\mathrm{B}}$ and $\Theta_{\mathrm{p}} = +7.8(2)$ K for the CO-LNMO sample. If we assume that Ni^{2+} ions are in the $S = 1$ ($t_{2g}^6 e_g^2$) state, Mn^{4+} ions are in the $S = 3/2$

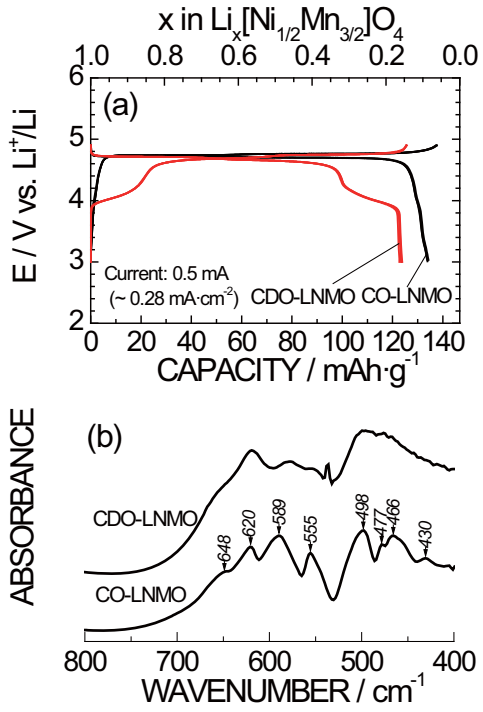

Fig. 12 (a) Charge and discharge curves of lithium cells with both CDO-LNMO and CO-LNMO. The cells were operated in the voltage range between 3 and 5 V at a current density of 0.28 mA·cm^{-2} at 25°C. (b) FTIR spectra for the CDO-LNMO and CO-LNMO samples. The more than eight absorption bands in (b) indicate that the space group symmetry of CO-LNMO is lower than $Fd\bar{3}m$.

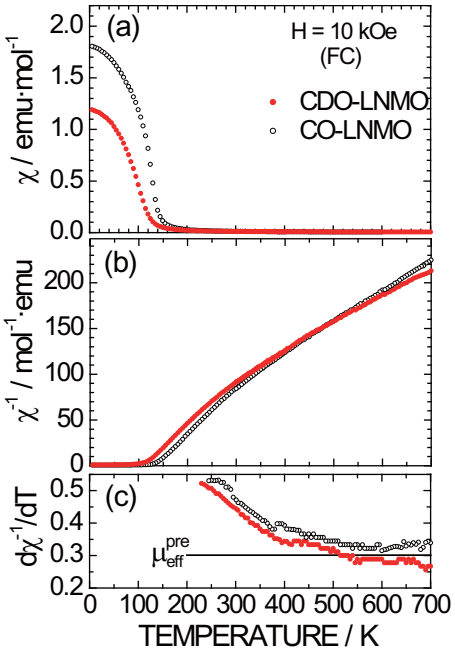

Fig. 13 Temperature (T) dependence of (a) χ, (b) χ^{-1}, and (c) the slope of χ^{-1} ($d\chi^{-1}/dT$) for the CDO-LNMO and CO-LNMO samples. χ was measured in FC mode with $H = 10$ kOe. The solid line in (c) represents the predicted effective magnetic moment ($\mu_{\mathrm{eff}}^{\mathrm{pre}}$) calculated assuming that Ni^{2+} ions are in the $S = 1$ ($t_{2g}^6 e_g^2$) state, Mn^{4+} ions are in the $S = 3/2$ ($t_{2g}^3 e_g^0$) state, and $g = 2$.

($t_{2g}^3 e_g^0$) state, and the gyromagnetic constant $g = 2$, then the spin-only effective magnetic moment (μ_{eff}^{pre}) for $Li[Ni_{1/2}^{2+}Mn_{3/2}^{4+}]O_4$ is predicted to be 3.64 μ_B. The μ_{eff} obtained for both samples are almost consistent with μ_{eff}^{pre}, although μ_{eff} for CDO-LNMO is slightly larger than that for CO-LNMO. Here, we wish emphasize that the $\chi(T)$ curves typically reported for $Li[Ni_{1/2}Mn_{3/2}]O_4$ below 400 K[71-73] provide an incorrect estimation of both μ_{eff} and Θ_p.

Figure 14(a) shows the T dependence of χ for the CDO-LNMO and CO-LNMO samples in both ZFC and FC modes with H = 100 Oe. $Li[Ni_{1/2}Mn_{3/2}]O_4$ is already known to undergo a ferrimagnetic transition at around T_C = 130 K; the spin arrangements of both Ni^{2+}-Ni^{2+} and Mn^{4+}-Mn^{4+} ions are FM, but that of Ni^{2+}-Mn^{4+} ions is AF.[74] As T decreases from 150 K, χ_{FC} for the CO-LNMO sample rapidly deviates from χ_{ZFC} at ca. 130 K, which indicates a sharp ferrimagnetic transition. In contrast, the magnetic behavior for CDO-LNMO is very different from that for CO-LNMO and is classified as P-type ferrimagnetism.[43] That is, as T decreases from 150 K, χ_{ZFC} starts to deviate from χ_{FC} below ca. 120 K and reaches a broad maximum at ca. 50 K, which suggests that a ferrimagnetic contribution except for the interaction between Ni^{2+} and Mn^{4+} ions, and/or a spin-glass-like contribution occur in the sample. Figure 14(b) shows that the M-H curve for the CO-LNMO sample at 5 K exhibits a typical loop of a soft ferromagnet, i.e., M rapidly increases with increasing H and levels off at 18.5 × 10^3 emu·mol^{-1}, even at $H \leq 5$ kOe. If we assume that $Li[Ni_{1/2}Mn_{3/2}]O_4$ is ferrimagnetic, the spin-only net magnetic moment (μ_{net}^{pre}) is calculated to be 3.5 μ_B using the following relation:

$$\mu_{net}^{pre} = S_{Mn} \times g \times 3/2 - S_{Ni} \times g \times 1/2 \quad \cdots\cdots\cdots (10)$$

where S_{Mn} = 3/2, S_{Ni} = 1, and g = 2. The net magnetic moment (μ_{net}) for the CO-LNMO sample at H = 55 kOe (= 3.31 μ_B) is very close to μ_{eff}^{pre} (= 3.5 μ_B). Although M for the CDO-LNMO sample does not saturate even at H = 55 kOe, μ_{net} is calculated to be 2.40 μ_B from M at H = 55 kOe.

It is difficult to identify $Li[Ni_{1/2}Mn_{3/2}]O_4$ ($P4_332$) from the CDO-LNMO phase using μ_{eff}, because μ_{eff} = 3.78(1) μ_B for CDO-LNMO and μ_{eff} = 3.50(1) μ_B for CO-LNMO. However, the M-H curve clearly reveals a characteristic feature of $Li[Ni_{1/2}Mn_{3/2}]O_4$ ($P4_332$). The M-H curve for CO-LNMO has an FM hysteresis with a saturation magnetization (M_s) ~ 3.31 μ_B. This value is almost consistent with μ_{eff}^{pre} (= 3.5 μ_B). Here, M_s for $Li[Ni_{1/2}Mn_{3/2}]O_4$ were also reported by several authors: 19.2 × 10^3 emu·mol^{-1} (≈ 3.44 μ_B) at 5 K,[71] 17.3 × 10^3 emu·mol^{-1} (≈ 3.10 μ_B) at 2 K,[72] and 16.5 × 10^3 emu·mol^{-1} (≈ 2.96 μ_B) at 4 K.[73] Although there were no electrochemical data in the latter two reports, the charge/discharge curves for the former $Li[Ni_{1/2}Mn_{3/2}]O_4$ showed a rechargeable capacity above 130 mAh·g^{-1} with a flat operating voltage at around 4.7 V.[71] Figure 14(b) shows that M at H = 55 kOe for CDO-LNMO is decreased to ca. 13.4 × 10^3 emu·mol^{-1} (≈ 2.40 μ_B). Therefore, the discrepancy between the observed μ_{net} and μ_{eff}^{pre} should be attributed to the cation-disordering of $Li[Ni_{1/2}Mn_{3/2}]O_4$, although this has not been claimed in the previous reports on the magnetism of $Li[Ni_{1/2}Mn_{3/2}]O_4$.[71-73] In other words, we can quantitatively examine the degree of cation-ordering in the $Li[Ni_{1/2}Mn_{3/2}]O_4$ sample using μ_{net},[38]

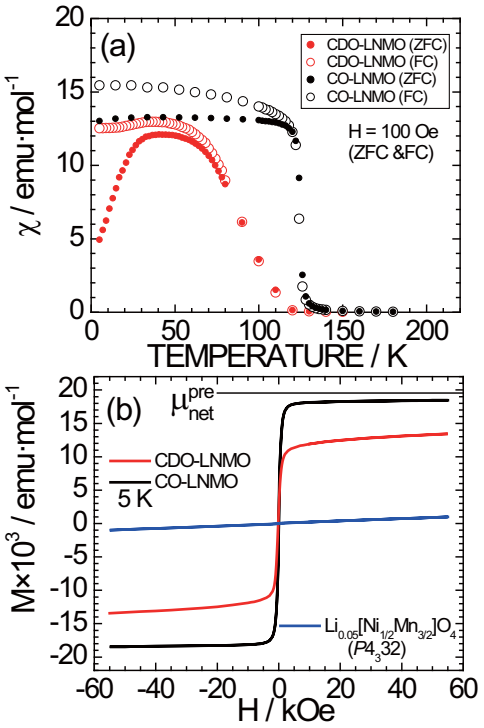

Fig. 14 (a) Temperature dependence of χ for the CDO-LNMO and CO-LNMO samples measured in ZFC and FC modes with H = 100 Oe. (b) M as a function of H for the CDO-LNMO and CO-LNMO samples. The solid lines indicate the predicted spin-only net magnetic moment (μ_{eff}^{pre}) calculated assuming that $Li[Ni_{1/2}Mn_{3/2}]O_4$ is ferrimagnetic, the spin arrangements of both Ni^{2+}-Ni^{2+} and Mn^{4+}-Mn^{4+} ions are FM, but that of Ni^{2+}-Mn^{4+} ions is AF.

as in the XRD analysis of $LiNiO_2$ for which the integrated XRD peak ratio of $I(003)/I(104)$ is a good indicator for the occupancy of Ni ions in the Li layers.[7] It should be noted that the highly crystallized $Li[Ni_{1/2}Mn_{3/2}]O_4$ compound was synthesized by a two-step solid-state reaction; well cation-ordering in $Li[Ni_{1/2}Mn_{3/2}]O_4$ is prepared by annealing the cation-disordering $Li[Ni_{1/2}Mn_{3/2}]O_4$ compound.[15,39] To produce a large amount of $Li[Ni_{1/2}Mn_{3/2}]O_4$ in the future, it is important to identify the quality of $Li[Ni_{1/2}Mn_{3/2}]O_4$ before measuring the electrochemical properties, and χ measurements are expected to be a powerful tool for such a purpose.

Besides LIB applications, $Li[Li_{1/2}Mn_{3/2}]O_4$ ($P4_332$) is a subject of considerable interest with respect to magnetism, because Ni and Mn ions form a three-dimensional array of corner-sharing tetrahedral, and thus satisfy one of the conditions for geometrical frustration. Figure 14(b) shows an *M-H* curve for the delithiated $Li_{0.05}[Ni_{1/2}Mn_{3/2}]O_4$ sample, which is prepared from the CO-LNMO sample by electrochemical reaction.[37] Although a small FM component is observed within $H \leq 5$ kOe, M increases almost linearly with H up to 55 kOe. The $M(H)$ curve for $Li_{0.05}[Ni_{1/2}Mn_{3/2}]O_4$ is very similar to that for λ-MnO_2 ($Li_0Mn_2O_4$),[37] so that the $Li_{0.05}[Ni_{1/2}Mn_{3/2}]O_4$ sample is considered to be in a PM or AF state even at 5 K.

The ionic distribution and spin arrangement of $Li_0[Ni^{4+}_{1/2}Mn^{4+}_{3/2}]O_4$ are the same as those for $Li[Mg^{2+}_{1/2}Mn^{4+}_{3/2}]O_4$[36] and $Li_{1/2}Zn_{1/2}[Li^{+}_{1/2}Mn^{4+}_{3/2}]O_4$;[74,75] the Mn^{4+} ions are located at the 12*d* sites of the spinel lattice with $P4_332$ space group, and the Ni^{4+}, Mg^{2+}, and Li^+ ions are non-magnetic. Both *M-H* curves for $Li[Mg_{1/2}Mn_{3/2}]O_4$ ($P4_332$) and $Li_{1/2}Zn_{1/2}[Li_{1/2}Mn_{3/2}]O_4$ ($P2_13$) exhibit soft FM behavior below $T_C = 20$ K[36] and $T_C = 22$ K[75], respectively; therefore, the $M(H)$ curve for the $x = 0.05$ sample is very different from those for $Li[Mg_{1/2}Mn_{3/2}]O_4$ and $Li_{1/2}Zn_{1/2}[Li_{1/2}Mn_{3/2}]O_4$.

The different magnetic behavior between $Li_{0.05}[Ni_{1/2}Mn_{3/2}]O_4$ and $Li[Mg_{1/2}Mn_{3/2}]O_4$ (and $Li_{1/2}Zn_{1/2}[Li_{1/2}Mn_{3/2}]O_4$) could be explained by the dependence of magnetic interactions on the cubic lattice parameter a_c, i.e., the distance between Mn^{4+} ions ($r_{Mn\text{-}Mn}$). If we consider only the first nearest neighbor (nn) coupling constant (J_1) and ignore the coupling between the second and higher nn, then the 90° superexchange Mn^{4+}-O^2-Mn^{4+} ($J_{1,s}$) interaction should be FM, whereas direct Mn^{4+}-Mn^{4+} ($J_{1,d}$) interaction should be AF.[76] This means that the magnetic behavior of $Li_x[M_{1/2}Mn^{4+}_{3/2}]O_4$ (M = Mg, Ni, and Mn) is determined by competition between $J_{1,d}$ and $J_{1,s}$. Here, the distance between Mn^{4+} ions ($r_{Mn\text{-}Mn}$) at ca. 293 K is calculated as 2.882 Å for $Li[Ni_{1/2}Mn_{3/2}]O_4$,[15,37,38] 2.888 Å for $Li[Mg_{1/2}Mn_{3/2}]O_4$,[36] 2.887 Å for $Li_{1/2}Zn_{1/2}[Li_{1/2}Mn_{3/2}]O_4$,[75] 2.820 Å for $Li_0[Ni_{1/2}Mn_{3/2}]O_4$,[15,37] and 2.833 Å for λ-MnO_2.[37,40,42] Therefore, it is likely that $J_{1,s}$ is dominant for $Li[Ni_{1/2}Mn_{3/2}]O_4$ and $Li[Mg_{1/2}Mn_{3/2}]O_4$, while $J_{1,d}$ is dominant for $Li_0[Ni_{1/2}Mn_{3/2}]O_4$ and λ-MnO_2. Such a variation from FM to AF ordering with a_c is also observed for a series of chromium spinels, ACr_2X_4 (A = Mg, Zn, and Cd: X = O, S, and Se)[77], in which the Cr^{3+} ions are in the $S = 3/2$ ($t^3_{2g}e^0_g$) state; $CdCr_2S_4$ with $r_{Cr\text{-}Cr} = 3.61$ Å is FM ($T_C = 85$ K), and $CdCr_2O_4$ with $r_{Cr\text{-}Cr} = 3.03$ Å is AF ($T_N = 9$ K).

3. 4 Comparison between Electrochemical and Chemical Delithiated Reactions[40-42]

Although a non-aqueous electrolyte is used in current LIBs, it is widely recognized that acid treatment with an aqueous solution produces a fully delithiated phase. Hunter reported[78] that fully delithiated $Li_xMn_2O_4$ (λ-MnO_2) is prepared by immersion of $LiMn_2O_4$ in an acid solution according to the following disproportionation reaction:

$$4LiMn^{3+}Mn^{4+}O_4(\text{sol.}) + 8H^+ \rightarrow 6\lambda - Mn^{4+}O_2(\text{sol.}) + 2Mn^{2+}(\text{liq.}) + 4Li^+ + 4H_2O \quad \cdots\cdots\cdots\cdots (11)$$

This is because acid treatment in a solution with sufficient H^+ corresponds to the voltage 1.23 V vs. standard hydrogen electrode (SHE) and is eventually equivalent to the electrochemical charging up to ca. 4.2 V vs. Li^+/Li.[79] However, the chemical delithiation process should be different from the electrochemical delithiation process, because the disproportionation reaction described in Eq. (11) always involves dissolution from a particle, and consequently, the solid-liquid interface is renewed during the reaction. Thus, we have investigated the structural and magnetic natures of both electrochemically (EC-) and chemically (C-) prepared $Li_xMn_2O_4$ and Li_xNiO_2 samples by XRD, χ, μSR, and thermal analyses.

Figure 15 shows the T dependence of χ^{-1} for the $Li_xMn_2O_4$ and Li_xNiO_2 samples prepared by both EC- and C-reactions. χ was measured in FC mode with $H = 10$ kOe. The $\chi^{-1}(T)$ curve for C-$Li_{0.07}Mn_2O_4$ is

almost the same as that for EC-$Li_{0.03}Mn_2O_4$. As T decreases from 350 K, the $\chi^{-1}(T)$ curves for all samples exhibit Curie-Weiss paramagnetic behavior down to ca. 200 K, except for the cusp at T_{JT} (= 285 K). Using Eq. (9) in the T range between 200 and 350 K, values of μ_{eff} and Θ_p were obtained for the $Li_xMn_2O_4$ samples and are given in **Table 1**. Here, μ_{eff}^{pre} is calculated under the assumption that Mn^{3+} ions are in the high-spin state with $S = 2$ ($t_{2g}^3e_g^1$), Mn^{4+} ions with $S = 3/2$ ($t_{2g}^3e_g^0$), and $g = 2$. μ_{eff} obtained for both the EC-$Li_{0.03}Mn_2O_4$ and C-$Li_{0.07}Mn_2O_4$ samples are very close to μ_{eff}^{pre}, so that μ_{eff} for both samples are well explained by the Mn valence estimated from the Li/Mn ratio. Figure 15(b) shows that the $\chi^{-1}(T)$ curve for C-$Li_{0.01}NiO_2$ is very different from that for EC-$Li_{0.05}NiO_2$; the magnitude of χ^{-1} for C-$Li_{0.01}NiO_2$ is smaller than that for EC-$Li_{0.05}NiO_2$ in the entire T range measured. Furthermore, as given in Table 1, μ_{eff} for C-$Li_{0.01}NiO_2$ (= 1.43 μ_B) is approximately twice that for EC-$Li_{0.05}NiO_2$ (= 0.71 μ_B). Here, μ_{eff} for $LiNiO_2$ is larger by 0.3 μ_B than μ_{eff}^{pre}, which is calculated by the assumption that Ni^{3+} and Ni^{4+} ions are in the low-spin state with $S = 1/2$ ($t_{2g}^6e_g^1$) and $S = 0$ ($t_{2g}^6e_g^0$), respectively, and $g = 2$. The difference between μ_{eff} and μ_{eff}^{pre} is probably due to an enhancement of the g-factor caused by local JT distortion of the NiO_6-octahedra.[80] Thus, the average valence for C-$Li_{0.01}NiO_2$ is not simply determined by the Li/Ni ratio, even if we consider enhancement of the g-factor and/or analytical error in the Li/Ni ratio of the ICP-AES analysis data ($\delta x = 0.01$).[40]

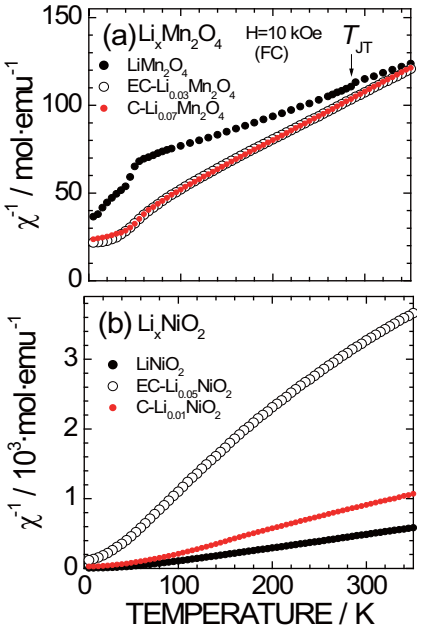

Fig. 15 Temperature dependence of χ^{-1} for (a) $Li_xMn_2O_4$ and (b) Li_xNiO_2 samples measured in FC mode with H = 10 kOe. The EC-$Li_{0.03}Mn_2O_4$ and EC-$Li_{0.05}NiO_2$ samples were prepared by electrochemical (EC-) reaction, while the C-$Li_{0.07}Mn_2O_4$ and C-$Li_{0.01}NiO_2$ samples were prepared by chemical (C-) reaction. T_{JT} represents the Jahn-Teller (JT) transition temperature.

According to the structural analyses of $Li_xMn_2O_4$ and Li_xNiO_2, the oxygen stacking sequence for $Li_xMn_2O_4$ is maintained in the *ccp* structure down to $x \approx 0$.[42,78] However, those for both EC-Li_xNiO_2[65] and C-Li_xNiO_2[66] are partially converted from the *ccp* structure to the *hcp* structure below $x \approx 0.1$. Note that proton insertion materials such as NiOOH and CoOOH for Ni-MH batteries have the *hcp* structure with an ABAB oxygen stacking sequence, while lithium insertion materials such as $LiNiO_2$ (NiOOLi) and $LiCoO_2$ (CoOOLi) for LIBs have the *ccp* structure with an ABCABC oxygen stacking sequence. Thus, the structural variation from the *ccp* to *hcp* structure in Li_xNiO_2 with $x \leq 0.1$ naturally induces proton insertion into the material.

Figure 16(a) shows the T dependence of N_{ATF} for the EC-$Li_{0.10}NiO_2$ and C-$Li_{0.01}NiO_2$ samples obtained by wTF-μSR measurements. For the EC-$Li_{0.10}NiO_2$ sample, as T decreases from 50 K, N_{ATF} is ca. 1 down to ca. 20 K, then slightly decreases by ca. 0.1 with further decrease in T, which is consistent with the majority non-magnetic 4+ state of the Ni ions with

Table 1 Effective magnetic moment (μ_{eff}) and Curie-Weiss temperature (Θ_p) for $Li_xMn_2O_4$ and Li_xNiO_2.

Sample[a]	μ_{eff} / μ_B[b]	Θ_p / K[b]	μ_{eff}^{pre} / μ_B[c]
$LiMn_2O_4$	4.40(2)	-260(5)	4.42
EC-$Li_{0.03}Mn_2O_4$	3.80(2)	-89(2)	3.89
C-$Li_{0.07}Mn_2O_4$	3.85(2)	-98(3)	3.91
$LiNiO_2$	2.03(1)	49(1)	1.73
EC-$Li_{0.05}NiO_2$	0.71(1)	24(2)	0.43
C-$Li_{0.01}NiO_2$	1.43(9)	46(2)	0.17

[a] $Li_xMn_2O_4$ and Li_xNiO_2 samples were prepared by both electrochemical (EC-) and chemical (C-) reactions.
[b] The values of μ_{eff} and Θ_p were obtained by fitting the χ vs. T curve in the T range between 200 and 350 K.
[c] μ_{eff}^{pre} is the predicted effective magnetic moment for $Li_xMn_2O_4$ and Li_xNiO_2 calculated assuming that Mn^{3+} ions are in the high-spin state with $S = 2$ ($t_{2g}^3e_g^1$), Mn^{4+} ions with $S = 3/2$ ($t_{2g}^3e_g^0$), Ni^{3+} ions with $S = 1/2$ ($t_{2g}^6e_g^0$), Ni^{4+} ions with $S = 0$ ($t_{2g}^6e_g^0$), and $g = 2$.

$S = 0$ ($t_{2g}^6 e_g^0$). For the C-$Li_{0.01}NiO_2$ sample, as T decreases from 50 K, the $N_{ATF}(T)$ curve shows two step-like drops at ca. 15 K and below 10 K, although $N_{ATF} = 0.32$ even at 1.8 K. This indicates that (*i*) magnetic Ni ions are still present in the sample, as expected from the value of μ_{eff}, (*ii*) there are at least three different magnetic phases denoted as M1, M2, and M3 in the sample, and (*iii*) approximately 1/3 of the sample is still PM even at 1.8 K. Figure 16(b) shows the ZF-μSR spectra for the EC-$Li_{0.10}NiO_2$ and C-$Li_{0.01}NiO_2$ samples at 15 at 12.5 K, respectively. Note that both samples are in the PM state, as shown in Fig. 16(a). In the PM state, muon-spins should be depolarized by the randomly oriented nuclear magnetism, not by the electronic magnetism. Therefore, the ZF-μSR spectrum is fitted by a dynamic KT[47] function, $G^{DGKT}(t, \Delta, \nu)$:

$$A_0 P_{ZF}(t) = A_{KT} G^{DGKT}(\Delta, \nu, t) + A_{fast} \exp(-\lambda_{fast} t), \quad \cdots\cdots\cdots\cdots (12)$$

where A_{KT} and A_{fast} are the asymmetries of the KT (PM) phase and residual magnetic phase, respectively, and λ_{fast} is the relaxation rate of the magnetic phase.

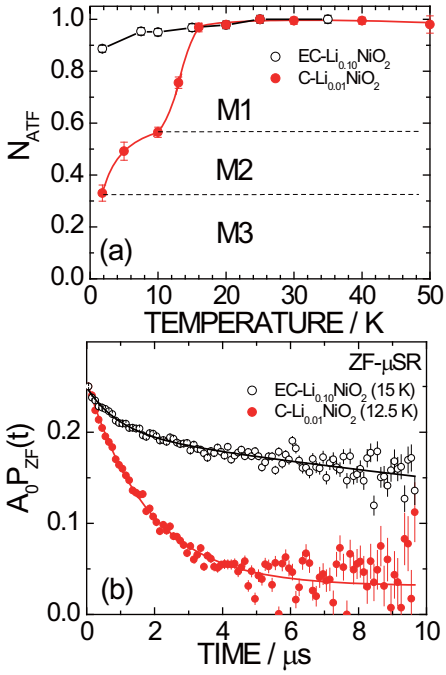

Fig. 16 (a) Temperature dependence of the normalized wTF-asymmetries (N_{ATF}) for the EC-$Li_{0.10}NiO_2$ and C-$Li_{0.01}NiO_2$ samples. (b) ZF-μSR spectra for the EC-$Li_{0.10}NiO_2$ sample at 15 K and for the C-$Li_{0.01}NiO_2$ sample at 12.5 K. The solid lines in (b) indicate the fitting results from Eq. (12).

The ZF-μSR spectrum for EC-$Li_{0.10}NiO_2$ shows a slow relaxation, which indicates that muon-spins are mainly depolarized by the nuclear magnetic moment of Li. In contrast, the ZF-μSR spectrum for C-$Li_{0.01}NiO_2$ shows a large relaxation. Δ, which corresponds to the internal magnetic field, is calculated as 0.075(2) μs^{-1} at 12.5 K for the EC-$Li_{0.10}NiO_2$ sample, while it is calculated as 0.355(3) μs^{-1} at 15 K for the C-$Li_{0.01}NiO_2$ sample. Note that the C-$Li_{0.01}NiO_2$ sample is almost fully delithiated. This indicates that there is another origin for the large relaxation observed only for the C-$Li_{0.01}NiO_2$ sample. The nuclear magnetic moment caused by both the O and Ni nuclei is negligibly small; therefore, the large relaxation for the C-$Li_{0.01}NiO_2$ sample is most likely due to the nuclear magnetic moment of the ^1H nucleus. Thus, the μSR result suggests the presence of H^+ ions in the C-$Li_{0.01}NiO_2$ sample, although a proton-free model was previously proposed for C-Li_xNiO_2.[66]

In order to confirm the absence/presence of oxygen deficiency and H^+ ions, thermogravimetry (TG) and pyrolysis gas chromatography/mass spectroscopy (Py-GC/MS) analyses were conducted. **Figure 17**(a) shows the TG curve for the C-$Li_{0.01}NiO_2$ sample. As T increases from ambient T, the TG curve decreases slightly above ca. 380 K, then decreases significantly around 473 K, and finally maintains an almost constant value until 873 K. After the acid reaction, the C-$Li_{0.01}NiO_2$ sample was dried at only 40°C in an

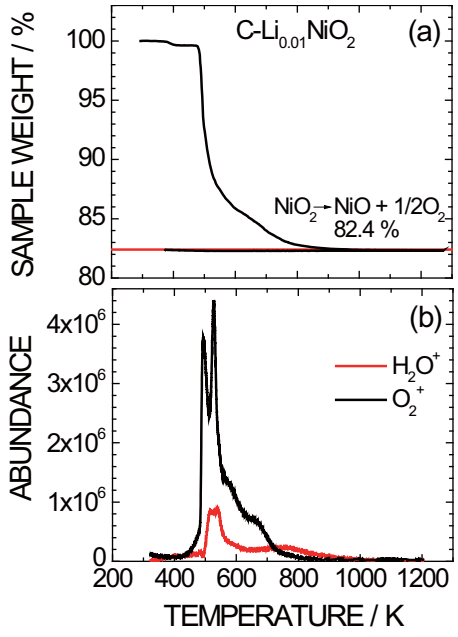

Fig. 17 (a) Thermogravimetric curve and (b) Py-GC/MS spectrum for the C-$Li_{0.01}NiO_2$ sample.

air-oven to avoid decomposition of the sample. Thus, the decrease around 380 K is most likely due to absorbed and/or adsorbed water. The weight loss at 1273 K (= m(1273 K) − m(300 K)) is ca. 17.7%, which is in good agreement with the expected change (= 17.6%) from the following oxygen evolution reaction:

$$NiO_2 \rightarrow NiO + 1/2O_2 \quad \cdots\cdots\cdots\cdots\cdots (13)$$

This suggests the absence of oxygen deficiencies in the C-$Li_{0.01}NiO_2$ sample, as reported previously.[66] Note that it is difficult to distinguish the absence/presence of H^+ ions in the C-$Li_{0.01}NiO_2$ sample from the TG curve, because the weight loss is calculated as ca. 81.5% for the $HNiO_2$ (NiOOH) composition.

In contrast, two spectral features, which are identified as O^{2+} (mass/charge = 32) and H_2O^+ (mass/charge = 18) ions, are clearly observed in the Py-GC/MS spectrum measured at 522 K (see Fig. 17(b)). This unambiguously demonstrates the presence of H^+ ions in the C-$Li_{0.01}NiO_2$ sample, which is consistent with the χ and μSR measurement results. Here, it should be noted that the trend for the H_2O^+ spectrum is very similar to that for the O^{2+} spectrum; both spectra show two peaks at ca. 490 and 535 K. This indicates that structurally bonded and/or intercalated water is present in the C-$Li_{0.01}NiO_2$ crystalline lattice. The TG curve for the $Ni(OH)_2$ compound showed two weight loss regions in the *T* ranges of 323-363 K and 453-723 K, which are attributed to dehydration reactions of absorbed/adsorbed water and structurally bonded/intercalated water, respectively. Therefore, the decomposition reaction for the C-$Li_{0.01}NiO_2$ sample is represented by:

$$H_xLi_{0.01}NiO_2 \cdot yH_2O \rightarrow H_xLi_{0.01}NiO_2 + yH_2O_2 \quad (380\text{-}470\ K) \cdots (14)$$

$$H_xLi_{0.01}NiO_2 \rightarrow Li_{0.01}NiO + x/2H_2O + (1 - x/4)O_2 \quad (470\text{-}870\ K) \cdots (15)$$

The total amount of H^+ ions in the C-$Li_{0.01}NiO_2$ sample is evaluated as ca. 0.5, i.e. $H_{\sim 0.5}Li_{0.01}NiO_2$, from the linear relationship between μ_{eff} and *x* in the EC-Li_xNiO_2 sample. Thus, the vacant tetrahedral or octahedral sites in C-$Li_{0.01}NiO_2$ are partially occupied by H^+ ions. In this calculation, it was assumed that both Ni^{3+} and Ni^{4+} ions are in the low-spin state, because Ni ions occupy the octahedral sites in both the *ccp* and *hcp* structures. The results of wTF-μSR measurements also support this assumption; Fig. 16(a) indicates that three different magnetic phases of M1, M2, and M3 are present according to the *T* dependence of N_{ATF}, which indicates the inhomogeneity of the sample. The volume fraction of the M1, M2, and M3 phases is approximately 40, 30, and 30%, respectively. T_m of the M1 (M2) phase is almost the same as that for the EC-$Li_{0.60}NiO_2$ (EC-$Li_{0.50}NiO_2$) sample;[32,33,41] therefore, the average valence of Ni ions (V_{Ni}^{ave}) for the C-$Li_{0.01}NiO_2$ sample is estimated as ca. 3.6 (= 4 − 0.6 × 0.4 − 0.5 × 0.3). This is consistent with the χ measurement results ($V_{Ni}^{ave} \sim 3.5$). We emphasize that the detection of H^+ ions in LIB materials is significantly important for improvement of the cycling and storage performance at elevated temperatures above 55°C. This is because electrochemical charging at high voltages above 4.2 V sometimes generates H^+ ions, which results from the decomposition of non-aqueous electrolytes, such as the case for Li_2MnO_3.[81] χ and μSR are therefore powerful techniques to investigate such phenomena.

4. Conclusion

Magnetic susceptibility (χ) analysis and muon-spin rotation/relaxation (μSR) spectroscopy were used to elucidate the electrochemical reaction scheme of lithium insertion materials through their macro- and microscopic magnetic nature. A trial-and-error methodology is usually employed on an empirical basis to design advanced lithium insertion materials. However, the author believes that an in-depth understanding of the properties of materials can lead to the development of new functions or materials, because “Buds of science” come from growing “Why” in mind. Magnetic measurements are one such powerful tool to develop a deeper understanding of material properties.

Acknowledgements

This work was a collaboration with Dr. J. Sugiyama, Dr. Y. Ikedo, Dr. K. Kamazawa, and Dr. H. Nozaki of Toyota CRDL, Prof. T. Ohzuku and Dr. K. Ariyoshi of Osaka City University, Prof. K. Nishiyama and Dr. K. Shimomura of High Energy Accelerator Research Organization (KEK), Prof. J. H. Brewer of University of British Columbia, Prof. E. J. Ansaldo, Dr. G. D. Morris, and Dr. P. L. Russo of TRIUMF, Prof. K. H. Chow of University of Alberta, Dr. D. Andreica, Dr. A. Amato, and Dr. M. Månsson of Paul Scherrer Institut

(PSI), and Dr. I. Watanabe and Dr. T. Suzuki of RIKEN-Rutherford Appleton Laboratory (RIKEN-RAL). The author appreciates their experimental support and discussions. The author also thanks the staff of TRIUMF, PSI and RIKEN-RAL for their help with the μSR experiments. This work was partially supported by a Grant-in Aid for Scientific Research (B) (19340107) from the Ministry of Education, Culture, Sports, Science and Technology (MEXT) of Japan and the KEK-MSL Inter-University Program for Overseas Muon Facilities.

References

(1) Pistoia, G., *Lithium Batteries* (1993), Elsevier.
(2) Mizushima, K., Jones, P. C., Wiseman, P. J. and Goodenough, J. B., *Mater. Res. Bull*., Vol.15 (1980), p.783.
(3) Nagaura, T. and Tozawa, K., *Prog. Batt. Solar Cells*, Vol.9 (1990), p.209.
(4) Reimers, J. N. and Dahn, J. R., *J. Electrochem. Soc*., Vol.139 (1992), p.2091.
(5) Ohzuku, T. and Ueda, A., *J. Electrochem. Soc.*, Vol.141 (1994), p.2972.
(6) Dahn, J. R., von Sacken, U. and Michal, C. A., *Solid State Ionics*, Vol.44 (1990), p.87.
(7) Ohzuku, T., Ueda, A. and Nagayama, M., *J. Electrochem. Soc.*, Vol.140 (1993), p.1862.
(8) Rougier, A., Gravereau, P. and Delmas, C., *J. Electrochem. Soc.*, Vol.143 (1996), p.1168.
(9) Delmas, C. and Saadoune, I., *Solid State Ionics*, Vol.53-56 (1992), p.370.
(10) Ohzuku, T., Nakura, T. and Aoki, T., *Electrochim. Acta*, Vol.45 (1999), p.151.
(11) Thackeray, M. M., Mansuetto, M. F., Dees, D. W. and Visseres, D. R., *Mater. Res. Bull.*, Vol.21 (1996), p.133.
(12) Gao, Y. and Dahn, J. R., *J. Electrochem. Soc.*, Vol.143 (1996), p.1783.
(13) Amatucci, G. and Tarascon, J.-M., *J. Electrochem. Soc.*, Vol.149 (2002), p.K31.
(14) Zhong, Q., Bonakdarpour, A., Zhang, M., Gao, Y. and Dahn, J. R., *J. Electrochem. Soc.*, Vol.144 (1997), p.205.
(15) Ariyoshi, K., Iwakoshi, Y., Nakayama, N. and Ohuzku, T., *J. Electrochem. Soc.*, Vol.151 (2004), p.A296.
(16) Kunduraci, M. and Amatucci, G. G., *J. Electrochem. Soc.*, Vol.153 (2006), p.A1345.
(17) Padhi, A. K., Nanjundaswamy, K. S. and Goodenough, J. B., *J. Electrochem. Soc*., Vol.144 (1997), p.1188.
(18) Yamada, A., Chung, S. C. and Hinokuma, K., *J. Electrochem. Soc*., Vol.148 (2001), p.A224.
(19) Saadoune, I. and Delmas, C., *J. Mater. Chem.*, Vol.6 (1999), p.193.
(20) Gendron, F., Castro-Garcia, S., Popova, E., Ziolkiewicz, S., Soulette, F. and Julinen, C., *Solid State Inonics*, Vol.157 (2003), p.125.
(21) Sugiyama, J., Nozaki, H., Brewer, J. H., Ansaldo, E. J., Morris, G. D. and Delmas, C., *Phys. Rev. B*, Vol.72 (2005), 144424.
(22) Kikkawa, S., Miyazaki, S. and Koizumi, M., *J. Solid State Chem*., Vol.62 (1986), p.35.
(23) Ménétrier, M., Saadoune, I., Levasseur, S. and Delmas, C., *J. Mater. Chem*., Vol.9 (1999), p.1135.
(24) Schenck, A., *Muon Spin Rotation Spectroscopy* (1985), Adam Hilger.
(25) Mukai, K., Sugiyama, J., Ikedo, Y., Nozaki, H., Shimomura, K., Nishiyama, K., Ariyoshi, K. and Ohzuku, T., *J. Power Sources*, Vol.174 (2007), p.711.
(26) Mukai, K., Ikedo, Y., Sugiyama, J., Nishiyama, K., Andreica, D., Amato, A., Russo, P. L., Ansaldo, E. J., Brewer, J. H., Chow, K. H., Ariyoshi, K. and Ohzuku, T., *Phys. Rev. Lett.*, Vol.99 (2007), 087601.
(27) Mukai, K., Sugiyama, J., Ikedo, Y., Andareica, D., Amato, A., Brewer, J. H., Ansaldo, E. J., Russo, P. L., Chow, K. H., Ariyoshi, K. and Ohzuku, T., *J. Phys. Chem. Solids*, Vol.69 (2008), p.1479.
(28) Sugiyama, J., Mukai, K., Ikedo, Y., Nozaki, H., Månsson, M. and Watanabe, I., *Phys. Rev. Lett.* Vol.103 (2009), 147601.
(29) Mukai, K., Nozaki, H., Ikedo, Y., Sugiyama, J., Ariyoshi, K. and Ohzuku, T., *J. Power Sources*, Vol.192 (2009), p.684.
(30) Mukai, K., Sugiyama, J., Ikedo, Y., Brewer, J. H., Ansaldo, E. J., Morris, G. D., Ariyoshi, K. and Ohzuku, T., *J. Power Sources*, Vol.174 (2007), p.843.
(31) Mukai, K., Sugiyama, J. and Aoki, Y., *J. Solid State Chem*., Vol.183 (2010), p.1726.
(32) Mukai, K., Sugiyama, J., Ikedo, Y., Russo, P. L., Andreica, D., Amato, A., Ariyoshi, K. and Ohzuku, T., *J. Power Sources*, Vol.189 (2009), p.665.
(33) Sugiyama, J., Mukai, K., Ikedo, Y., Russo, P. L., Nozaki, H., Andreica, A., Amato, A., Ariyoshi, K. and Ohzuku, T., *Phys. Rev. B*, Vol.78 (2008), 144412.
(34) Sugiyama, J., Mukai, K., Ikedo, Y., Russo, P. L., Suzuki, T., Watanabe, I., Brewer, J. H., Chow, K. H., Ariyoshi, K. and Ohzuku, T., *Phys. Rev. B*, Vol.75 (2007), 174424.
(35) Mukai, K., Sugiyama, J., Ikedo, Y., Nozaki, H., Kamazawa, K., Andreica, D., Amato, A., Månsson, M., Brewer, J. H., Ansaldo, E. J. and Chow, K. H., *J. Phys. Chem. C*, Vol.114 (2010), p.11320.
(36) Mukai, K., Sugiyama, J., Ikedo, Y., Russo, P. L., Brewer, J. H., Ansaldo, E. J., Chow, K. H., Ariyoshi, K. and Ohzuku, T., *Physica B: Condened Matter*, Vol.404 (2009), p.656.
(37) Mukai, K. and Sugiyama, J., *Solid State Commun.*, Vol.150 (2010), p.906.
(38) Mukai, K. and Sugiyama, J., *J. Electrochem. Soc*., Vol.157 (2010), p.A672.
(39) Ohzuku, T., Ariyoshi, K. and Yamamoto, S., *J. Ceram. Soc. Jpn*., Vol.110 (2002), p.501.
(40) Mukai, K. and Sugiyama, J., *Chem. Lett.*, Vol.38 (2009), p.944.

(41) Mukai, K., Sugiyama, J., Ikedo, Y., Aoki, Y., Andreica, D. and Amato, A., *J. Phys. Chem. C*, Vol.114 (2010), p.8626.
(42) Mukai, K., Sugiyama, J., Kamazawa, K., Ikedo, Y., Andreica, D. and Amato, A., *J. Solid State Chem.*, Vol.184 (2011), p.1096.
(43) Chikazumi, S. and Charap, S. H., *Physics of Magnetism* (1978), Kreiger.
(44) Clarke, J. and Braginski, A. I., *The SQUID Handbook: Fundamentals and Technology of SQUIDs and SQUID Systems*, Vol.I (2004), WILEY-VCH.
(45) Sugiyama, J., *R&D Review of Toyota CRDL*, Vol.39 (2004), p.50.
(46) Chatterji, T., Henggeler, W. and Delmas, C., *J. Phys. Condens. Matter*, Vol.17 (2005), p.1341.
(47) Hayano, R. S., Umemura, Y. J., Imazato, J., Nishida, N., Yamazaki, T. and Kubo, R., *Phys. Rev. B*, Vol.20 (1979), p.850.
(48) Peres, J. P., Weill, F. and Delmas, C., *Solid State Ionics*, Vol.166 (1999), p.19.
(49) Arroyo y de Dompablo, M. E. and Ceder, G., *Chem. Mater*., Vol.15 (2003), p.63.
(50) Viciu, L., Bos., J. W. G., Zandbergen, H. W., Huang, Q., Foo, M. L., Ishikawa, S., Ramirez, A. P., Lee, M., Ong, N. P. and Cava, R. J., *Phys. Rev. B*, Vol.73 (2006), 174104.
(51) Foo, M. L., Wang, Y., Watauchi, S., Zandbergen, H. W., He, T., Cava, R. J. and Ong, N. P., *Phys. Rev. Lett.*, Vol.92 (2004), 247001.
(52) Watanabe, H., Mori, Y., Yokoi, M., Moyoshi, T., Soda, M., Yasui, Y., Kobayashi, Y., Sato, M., Igawa, N. and Kakurai, K., *J. Phys. Soc. Jpn.*, Vol.75 (2006), 034716.
(53) Sugiyama, J., Nozaki, H., Ikedo, Y., Mukai, K., Brewer, J. H., Ansaldo, E. J., Morris, G. D., Andreica, D., Amato, A., Fujii, T. and Asamitsu, A., *Phys. Rev. Lett.*, Vol.96 (2006), 037206.
(54) Lewis, M. J., Gaulin, B. D., Fikion, L., Kalin, C., Berlinsky, A. J., Dabkowsks, H. A., Qui, Y. and Copley, J. R. D., *Phys. Rev. B*, Vol.72 (2005), 014408.
(55) Sugiyama, J., Nozaki, H., Ikedo, Y., Mukai, K., Andreica, D., Amato, A., Brewer, J. H., Ansaldo, E. J., Morris, G. D., Takami, T. and Ikuta, H., *Phys. Rev. Lett.*, Vol.96 (2006), 197206.
(56) Yamada, A. and Tanaka, M., *Mater. Res. Bull.*, Vol.30 (1995), p.715.
(57) Sugiyama, J., Hioki, T., Noda, S. and Kontani, M., *J. Phys. Soc. Jpn*., Vol.66 (1997), p.1187.
(58) Rodriguez-Carvajal, J., Rousse, G., Masquelier, C. and Hervieu, M., *Phys. Rev. Lett.*, Vol.81 (1998), p.4660.
(59) Kaplan, M. D. and Vekhter, B. G., *Cooperative Phenomena in Jahn-Teller Crystals* (1995), Plenum Press.
(60) Storbel, P. and Lambert-Andron, B., *J. Solid State Chem.*, Vol.75 (1988), p.90.
(61) Takada, T., Hayakawa, H. and Akiba, E., *J. Solid State Chem.,* Vol.115 (1995), p.420.
(62) Takada, T., Akiba, E., Izumi, F. and Chakoumakos, B. C., *J. Solid State Chem.*, Vol.130 (1997), p.74.
(63) Kopec, M., Dygas, J. R., Krok, F., Mauger, A., Gendron, F. and Julien, C. M., *J. Phys. Chem. Solids*, Vol.69 (2008), p.955.
(64) Paulsen, J. M. and Dahn, J. R., *Chem. Mater.*, Vol.11 (1999), p.3065.
(65) Croguennec, L., Pouillerie, C. and Delmas, C., *J. Electrochem. Soc.*, Vol.147 (2000), p.1314.
(66) Arai, H., Tsuda, M., Saito, K., Hayashi, M., Takei, K. and Sakurai, Y., *J. Solid State Chem.*, Vol.163 (2002), p.340.
(67) Johnson, C. S., Li, N., Vaughey, J. T., Hackney, S. A. and Thackeray, M. M., *Electrochem. Commun.*, Vol.7 (2005), p.528.
(68) Thackeray, M. M., Johnson, C. S., Vaughey, J. T., Li, N. and Hckney, S. A., *J. Mater. Chem.*, Vol.15 (2005), p.2386.
(69) Meng, Y. S., Ceder, G., Grey, C. P., Yoon, W.-S., Jiang, M., Bréger, J. and Shao-Horn, Y., *Chem. Mater.*, Vol.17 (2005), p.2386.
(70) Bhagavantam, S. and Venkatarayudu, T., *Theory of Groups and Its Application to Physical Problems* (1969), Academic.
(71) Nakamura, T., Yamada, Y. and Tabuchi, M., *J. Appl. Phys*., Vol.98 (2005), 093905.
(72) Biskup, N., Matínez, J. L., Arroyo y de Dompablo, M. E., Díaz-Carrasco, P. and Morales, J., *J. Appl. Phys*., Vol.100, No.9 (2006), 093908.
(73) Amdouni, N., Zaghib, K., Gendron, F., Mauger, A. and Julien, C. M., *J. Magn. Magn. Mater.*, Vol.309 (2007), p.100.
(74) Blasse, G., *J. Phys. Chem. Solids*, Vol.27 (1966), p.383.
(75) Plumier, R. and Sougi, M., *J. Appl. Phys*., Vol.67 (1990), p.4787.
(76) Goodenough, J. B., *Magnetism and the Chemical Bond* (1963), Wiley.
(77) Baltzer, P. K., Wojtowicz, P. J., Robbins, M. and Lopatin, E., *Phys. Rev.*, Vol.151 (1967), p.367.
(78) Hunter, J. C., *J. Solid State Chem.*, Vol.39 (1981), p.142.
(79) Pourbaix, M., *Atlas of Electrochemical Equilibria in Aqueous Solutions* (1966), Pergamon.
(80) Yoshida, H., Muraoka, Y., Sörgel, T., Jansen, M. and Hiroi, Z., *Phys. Rev. B*, Vol.73 (2006), 020408.
(81) Robertson, A. D. and Bruce, P. G., *Chem. Mater*., Vol.15 (2003), p.1984.

Kazuhiko Mukai
Research Fields:
- Solid-state Electrochemistry
- Lithium-ion Battery

Academic Degree: Dr. Eng.
Academic Societies:
- American Chemical Society
- The Electrochemical Society
- The Electrochemical Society of Japan
- The Physical Society of Japan